Journal of Geophysical Research: Space Physics

RESEARCH ARTICLE
10.1002/2017JA024587

Formation of 30 KeV Proton Isotropic Boundaries During Geomagnetic Storms

S. Dubyagin[1], N. Yu. Ganushkina[1,2], and V. Sergeev[3]

[1]Finnish Meteorological Institute, Helsinki, Finland, [2]Climate and Space Sciences and Engineering Department, University of Michigan, Ann Arbor, MI, USA, [3]Department of Earth's Physics, St. Petersburg State University, St. Petersburg, Russia

Key Points:
- Conditions at equatorial part of proton Isotropic Boundary field lines are analyzed using TS05 magnetospheric model and THEMIS observations
- Adiabaticity parameter values expected for isotropic boundary formation by scattering on curved field lines were found for 60–80% of events
- Isotropic boundaries which do not fit this scenario reveal higher occurrence during the main phase or/and at latitudes lower than 59 degrees

Correspondence to:
S. Dubyagin,
stepan.dubyagin@fmi.fi

Citation:
Dubyagin, S., Ganushkina, N. Y., & Sergeev, V. A. (2018). Formation of 30 keV proton isotropic boundaries during geomagnetic storms. *Journal of Geophysical Research: Space Physics*, *123*, 3436–3459. https://doi.org/10.1002/2017JA024587

Received 12 JUL 2017
Accepted 20 MAR 2018
Accepted article online 26 MAR 2018
Published online 6 MAY 2018

Abstract We study the origin of the 30 keV proton isotropic boundary (IB) in the nightside auroral zone during geomagnetic storms, particularly, to address the recent results that the adiabaticity parameter K (ratio of the magnetic field line curvature radius to the particle gyroradius at the equator) on the IB field line can be much larger comparing to its theoretical estimate $K \sim 8$ for the field line curvature (FLC) scattering mechanism. During nine storms in 2011–2013, we investigate ~2,000 IBs observed by low-altitude Polar Operational Environmental Satellites (POES) satellites and apply the TS05 magnetospheric model to estimate the K value in the equatorial part of the IB field line. The statistical distribution of the estimated K parameter, while being rather broad, is centered on $K = 9–13$. For smaller subset of ~250 IBs, the concurrent magnetic field measurements on board Time History of Events and Macroscale Interaction During Substorms probes in the equatorial magnetotail were used to correct the estimated K-values accounting for the TS05 deviations from the real magnetic configuration. After correction, the K distribution becomes narrower, being still centered on $K = 9–12$. Different estimates give percentages of events with $K < 13$, which can be attributed to IBs formed by FLC scattering, between 60% and 80%. Finally, we have not found any dependence of the K distribution on magnetic local time and IB latitude, except for events with IB located at extremely low latitudes (<59°). These findings imply that the FLC scattering is a dominant mechanism of IB formation operating in a variety of magnetospheric conditions.

1. Introduction

The low-altitude observations of energetic particle fluxes always show the extended region of isotropic ion precipitation (e.g., Imhof et al., 1977; Søraas et al., 1977) which forms the proton auroral oval (Donovan, Jackel, Voronkov, et al., 2003). The low-latitude edge of this region is called the isotropic boundary (IB). This isotropic precipitation reveals a strong pitch angle diffusion, associated with violation of the first adiabatic invariant, which is capable to fill the loss cone during one traversal across the current sheet (Ganushkina et al., 2005; Sergeev et al., 1983, 1993). The IB delineates a boundary where the pitch angle scattering suddenly becomes less effective when moving inward, to lower latitude in the ionosphere, where the fluxes in the loss cone center become much lower than the fluxes of the locally trapped particles. The most frequently debated mechanisms of strong pitch angle scattering responsible for isotropic proton precipitation on the nightside include the field-line-curvature-related (FLC) scattering (e.g., Sergeev et al., 1983, 1993) and the scattering by electromagnetic ion cyclotron (EMIC) waves (e.g., Erlandson & Ukhorskiy, 2001; Kennel & Petschek, 1966; Liang et al., 2014).

A distinguishing feature of the FLC Petersburg a very robust and much better understood in comparison to wave-particle interaction process. The amplitude of pitch angle scattering depends on the ratio R_C/ρ where R_C is the magnetic field line curvature radius and ρ is the particle gyroradius in the current sheet center. It is beyond question that for $R_C/\rho \ll 10$, the adiabatic regime is severely violated and particle trajectories become chaotic in one particle current sheet crossing (Büchner & Zelenyi, 1989). This condition is fulfilled in the vast space of the tail plasma sheet outside $r \sim 12–15R_E$, naturally providing isotropic proton distributions in the plasma sheet (Wang et al., 2013) as well as extended isotropic precipitation in the proton auroral oval (Donovan, Jackel, Voronkov, et al., 2003). However, which particular mechanism is responsible for the proton precipitation in vicinity of the proton isotropy boundary is still under the discussion.

Analyses of charged particle trajectories in the simplified magnetic field models of the magnetotail current sheet (e.g., Delcourt et al., 1996; Sergeev et al., 1983) have shown that the condition for the complete loss

cone filling by FLC scattering is $K = R_C/\rho \leq 8$. This equation can be rewritten as

$$\frac{R_C}{\rho} \approx \frac{eB_Z^2}{mV\mathrm{d}B_r/\mathrm{d}Z} = \frac{eB_Z^2}{\sqrt{2mE}\mathrm{d}B_r/\mathrm{d}Z} \leq 8 \quad (1)$$

Here B_Z, B_r are the magnetic field Z and radial components, m, V, E are the particle mass, velocity, and energy, respectively. According to the relation (1), if the FLC scattering mechanism is responsible for the isotropy boundary formation, the IB location should strongly depend on the B_Z value in the conjugate current sheet. This prediction has a strong observational support (e.g., Donovan, Jackel, Klumpar, et al., 2003; Sergeev et al., 1993); it can be used for remote sensing of the magnetotail magnetic configuration. Another prediction of the FLC scattering mechanism is that for a typical magnetotail configuration with equatorial B_Z increasing monotonically toward the Earth, the IBs for low-energy particles has to be observed poleward from the IBs for high energy particles. Such energy dispersion, indeed, is predominantly seen in the nightside observations (Imhof et al., 1979; Sergeev, Chernyaeva, Apatenkov, et al., 2015). The inverse order of energy dispersion (called as "anomalous" dispersion), which is usually attributed to the wave-particle interaction process, can also be sometimes observed (Donovan, Jackel, Klumpar, et al., 2003; Liang et al., 2014; Sergeev, Chernyaeva, Apatenkov, et al., 2015). Unlike the FLC scattering mechanism, the particle interaction with EMIC waves theoretically can produce both types of the IB dispersion (Liang et al., 2014).

Different from FLC mechanism, the EMIC waves excitation and efficiency of the pitch angle scattering by EMIC waves depend on many factors (Kennel & Petschek, 1966; Usanova et al., 2016). Horne and Thorne (1993) showed theoretically that the plasmapause is a preferred location of EMIC waves excitations. Although this result was not fully supported observationally (Fraser & Nguyen, 2001), some authors did found on many occasions that the ions were scattered into loss cone by EMIC waves near the plasmapause (e.g., Xiong et al., 2016; Yahnin & Yahnina, 2007; Yuan et al., 2012). More generally, the theory predicts that EMIC wave excitation is favored by the presence of the cold ion population in addition to the anisotropic hot one (Gary et al., 1995) and that ion composition also plays a role (Kozyra et al., 1984). Meanwhile, the ambient magnetic field magnitude is also an important factor because it defines a particle resonance energy (Kennel & Petschek, 1966; Liang et al., 2014). Taken together, being dependent on combination of many different factors to provide the strong diffusion rate and isotropic precipitation, the wave-particle interaction is evaluated as much less probable (anyway, less frequent) player in isotropy boundary formation. This is supported by the fact that IBs are always observed at all magnetic local times (MLTs) and under any conditions, while the EMIC wave occurrence strongly depends on MLT and geomagnetic activity (Halford et al., 2010; Keika et al., 2013; Usanova et al., 2012).

For a long time since Sergeev et al. (1993), it was generally accepted that FLC scattering is the main mechanism of IB formation during low and moderate geomagnetic activity. This was questioned by the results of a few recent studies. In one approach, the statistics of standard and anomalous energy dispersion types was investigated. At low energies (1–20 keV), Liang et al. (2014) found numerous cases of the inverse proton energy dispersion and showed a couple of cases in which EMIC waves were directly observed in the equatorial magnetosphere in the sector where the inverse IB dispersion was identified. At higher proton energies (30 to 80 keV, which are preferable for remote sensing purposes), the situation seems to be different. According to large statistics presented in Sergeev, Chernyaeva, Apatenkov, et al. (2015), the inverse dispersion is rare ($\sim$ 5%); however, near the isotropy boundary, the precipitation was found to display a complicated structure in almost half of events, including coincident IBs in 30 and 80 keV proton energy channels, frequent multiple dropouts of precipitated-to-trapped flux ratio near the IB location, and observations of newly emerging isotropic precipitation equatorward of the previous IB, which are hard to explain with a simple FLC-based model. Uncertainty in the IB identification in such events may influence their interpretation; therefore, a further study of this aspect is desired.

Another approach to this problem is to verify experimentally the scattering condition (equation (1)), namely, evaluate magnetospheric conditions in the equatorial part of the magnetic field line on which the proton IB is observed, estimate the local K-value in that place, and compare this value to its theoretical prediction ($K = 8$). Generally, one has to use some magnetic field model to compute the K value and to preform mapping of the field line where the IB is observed. Various magnetospheric models have been used for this purpose, including the empirical models (e.g., Ganushkina et al., 2005), the adaptive empirical models (e.g., Kubyshkina et al., 1999; Pulkkinen et al., 1992; Sergeev, Chernyaeva, Angelopoulos, et al., 2015), and the magnetohydrodynamics (MHD) global magnetospheric simulations (Gilson et al., 2012; Ilie et al., 2015).

Accuracy of the model in representing the actual configuration is of the largest importance in such comparisons; the validation of the model's accuracy is also the least elaborated part of that kind of research. In two most recent attempts, it was found that the estimated K value distribution for 30 keV protons is shifted to much larger values compared to the theoretical $K = 8$. Median K values were 20 and 33, correspondingly, for 32 and 40 IB crossings considered in Sergeev, Chernyaeva, Angelopoulos, et al. (2015) and Ilie et al. (2015). This may imply that isotropy boundaries could be formed significantly inward from the $K = 8$ magnetic shell, suggesting a possible need of complementary proton scattering mechanisms in those regions acting, at least, in a significant percentage of cases. There were big differences in the models used (adaptive model and global MHD model, in Sergeev, Chernyaeva, Angelopoulos, et al. (2015) and Ilie et al. (2015), accordingly), as well as in the model validation (error estimation) tools applied in these papers, which makes a direct comparison of their results difficult. Anyway, the results of both studies cannot be generalized because the IB crossing data sets included a relatively small number of events and most of them occurred during quiet conditions.

An important aspect of the problem is the possible differences in the IB formation between quiet and storm times. Few studies specially addressed the peculiarities of the IB formation during storm periods though some authors used the storm time IBs in their studies assuming one or another mechanism of their formation (Asikainen et al., 2010; Søraas et al., 2002). Dubyagin et al. (2013) analyzed the nightside IBs observed during one storm event and found that the anomalous IB dispersion is mostly observed in the dusk sector (MLT 18–21) during the main phase of the storm. The statistical studies confirmed that the EMIC wave occurrence also peaks in the dusk sector during the main phase (Halford et al., 2010; Usanova et al., 2012). However, these authors found that the EMIC waves occurrence rate is quite low, especially for the inner magnetosphere (being less than 10% for 1 h MLT by $1R_E$ bin). Concerning the proton precipitation, Gvozdevsky et al. (1997) found that during and after strong magnetospheric disturbances, a weak pitch angle scattering (anisotropic precipitation) is seen equatorward from the IB. It might be speculated that for some events and/or in some regions, the wave-particle interaction can become so strong that the flux inside the loss cone would approach its value outside it, so that isotropic precipitation formed by the FLC scattering in the poleward part would merge with the isotropic precipitation caused by the wave-particle interaction process in the equatorial part. In such a case, the observed IB would be formed by such (yet unspecified) wave scattering mechanism. Also, Yahnin and Yahnina (2007) found that the source region of intense EMIC waves is often the localized region where the injected hot ions encounter the plasmasphere. However, although the ion injections are stronger and penetrate deeper during the storm periods, the plasmasphere also shrinks inward. Taking all these into consideration, it is not immediately obvious that the wave-related mechanism of the IB formation dominates during the geomagnetic storm periods. These aspects also need further study.

Our study is aimed to advance the understanding of the pitch angle scattering mechanism leading to the IB formation, with proper inclusion of the storm time periods. By analyzing the loss cone filling rate behavior near the IB, we take into account the uncertainty in possible identification of the isotropy boundaries and its dependence on the storm activity. Like in Sergeev, Chernyaeva, Angelopoulos, et al. (2015) and Ilie et al. (2015), we use the magnetospheric model to evaluate the K values in the magnetosphere and pay attention to the proper model validation; however, we do it on the larger statistics (thousands against a few tens of events) to evaluate statistically the most probable value of K parameter in our database.

Here we use the data of seven NOAA/POES low-orbital satellites to detect the isotropic boundaries near the midnight meridian during nine storm events. The brief description of data and instrumentation is presented in section 2. The data selection procedures are described in section 3.1. In section 3.2 we investigate statistical properties of the IB data set and present concise analysis of outliers. In section 3.3, we use the empirical models to estimate K parameter on the IB field line. To control the model accuracy, we use the concurrent measurements of the magnetic field in the equatorial magnetosphere on board Time History of Events and Macroscale Interaction During Substorms (THEMIS) spacecraft located at $R \leq 10R_E$. The detailed analysis of a few representative events is presented in section 3.4. The results are discussed and the conclusions are drawn in sections 4 and 5, respectively.

2. Data and Instrumentation

The low-altitude measurements are obtained from Space Environment Monitor-2 (SEM-2) (Evans & Greer, 2000) on board NOAA/POES satellites. SEM-2 consists of two detectors: (1) Total Energy Detector (TED) which measures energy flux of thermal protons and electrons in the energy range 50 eV–20 keV and (2) Medium

Table 1
List of Storm Events Selected for the Analysis

Date/Time	min(SYM-H)
2011-05-27/16:00:00, 2011-05-31/00:00:00	−94
2011-08-05/18:00:00, 2011-08-08/00:00:00	−126
2012-04-23/03:00:00, 2012-04-26/00:00:00	−125
2012-06-16/20:00:00, 2012-06-20/00:00:00	−69
2012-07-14/18:00:00, 2012-07-18/00:00:00	−123
2012-09-30/11:00:00, 2012-10-03/00:00:00	−138
2012-10-08/00:00:00, 2012-10-11/00:00:00	−116
2013-05-31/16:00:00, 2013-06-03/00:00:00	−137
2013-06-27/14:00:00, 2013-07-01/00:00:00	−111

Note. Dates are formatted as yyyy-mm-dd.

Energy Proton and Electron Detector (MEPED) which measures flux of the energetic protons and electrons from two orthogonal directions in a few energy channels. We use only two proton energy channels designated as P1 and P2, with nominal low-energy thresholds 30 and 80 keV, respectively. One MEPED proton telescope is oriented nearly along the local zenith, and it is referred to as 0° telescope because it measures precipitating particles with ∼0° pitch angles when a satellite is at the auroral latitudes. Another telescope points in a perpendicular direction, nearly in opposite direction to satellite velocity; it is referred to as 90° telescope, and it mostly detects the flux of locally trapped particles. This configuration allows the determination of the boundary between isotropic and anisotropic precipitations which is the focus of this study. The TED and MEPED detectors have a time resolution of 2 s, but the accumulation cycles of the 0° and 90° MEPED telescopes are offset by 1 s. For purely meridional orbits, the 2-s period corresponds to satellite displacement of ∼0.12° in latitude. We use the data from seven NOAA/POES satellites: NOAA-15 to NOAA-19 and METOP-01 and METOP-02. The data of METOP-01 satellite were available since October 2012, and NOAA-17 was not operating after April 2013. The satellites are positioned using the altitude-adjusted corrected geomagnetic (AACGM) coordinates (latitude and MLT) (Baker & Wing, 1989), computed using numerical field line tracing. The coordinates were adjusted to the geocentric distance $r = 1R_E$.

Magnetospheric observations come from the flux gate magnetometers (Auster et al., 2008) on board three innermost probes of THEMIS mission (Angelopoulos, 2008). The spin resolution (∼3 s) data were averaged over 1 min.

3. Data Analysis

3.1. Isotropic Boundary Selection

Since our study relies on the concurrent observations at low altitudes and in the equatorial magnetosphere, we selected nine storms during 2011–2013 when THEMIS apogees were on the nightside. These storms are listed in Table 1. They are moderate storms with peak SYM-H values around −100 nT. The 3–4-day long intervals include a sudden commencement (if it took place), the main phase, and one or two days of the recovery phase.

The isotropic boundaries were selected using a visual inspection of the data of the lowest energy channel (P1) of the MEPED proton detector. A nominal low-energy threshold of this channel is 30 keV, but the real energy can be somewhat higher due to the detector degradation (but always lower than the energy of P2 channel, see more details in Appendix A). In this study, we do not determine isotropic boundaries for P2 channel, and hence we do not analyze the IB energy-latitude dispersion. For P1 channel, we select only IBs within 21–03 h MLT. This limitation was imposed to concentrate on the region where the empirical models are expected to be the most accurate (e.g., magnetotail twist effect in presence of strong B_Y interplanetary magnetic field is minimal).

Since the storm time precipitations may have complicated structure, special caution should be taken when selecting IBs. Figure 1 shows four representative examples of the low-altitude proton flux observations during four different auroral region transits by METOP-02 and NOAA-19 satellites.

Figure 1a shows a typical latitudinal profile of the energetic proton fluxes. The isotropic precipitation from the plasma sheet is localized at latitude ∼62–72°. The low-latitude part (latitude ∼50–60°) is occupied by strongly

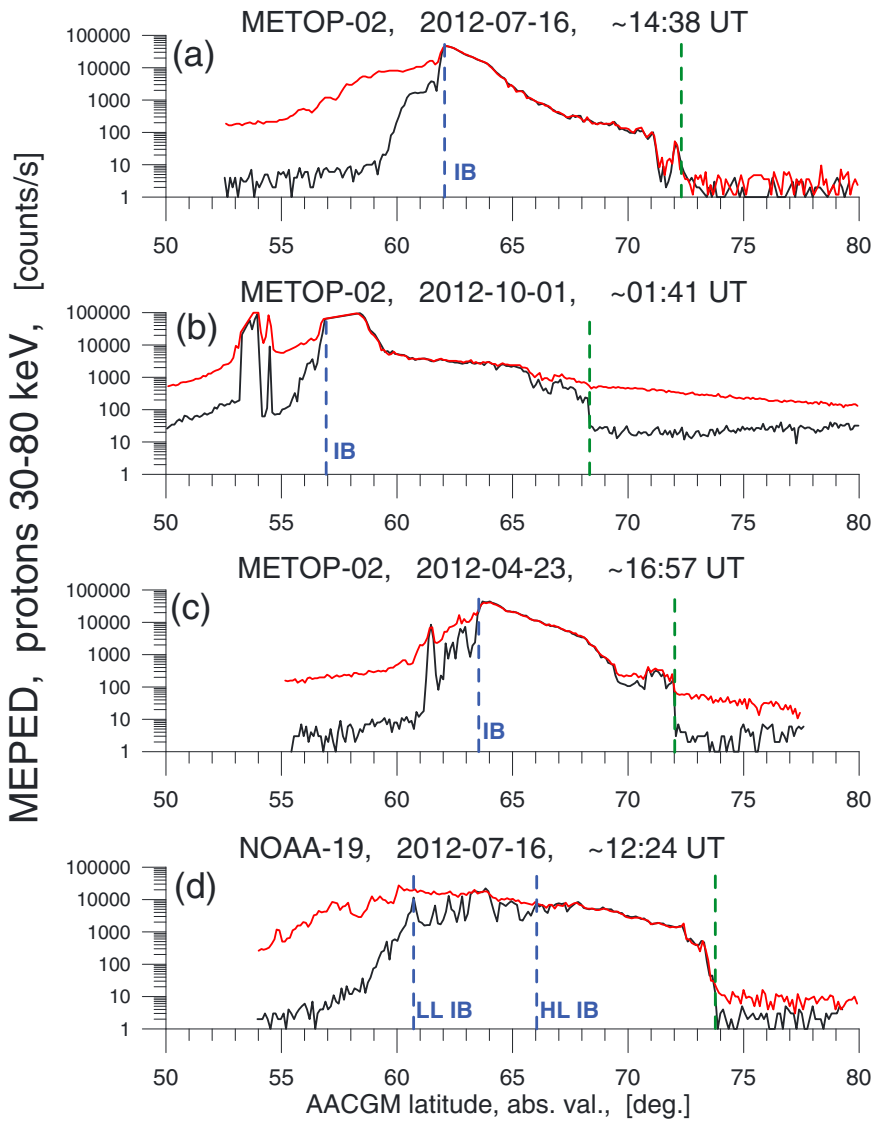

Figure 1. Examples of proton flux latitudinal profiles. The black and red lines show precipitating and locally trapped fluxes, respectively. The green and blue dashed vertical lines mark the polar cap boundary and isotropic boundary, respectively. In the bottom panel, two dashed blue lines mark the low-latitude and high-latitude limits of the IB determination uncertainty interval. MEPED = Medium Energy Proton and Electron Detector; AACGM = altitude-adjusted corrected geomagnetic.

anisotropic fluxes: the fluxes of the locally trapped particles (red line) are >2 order of magnitude higher than the fluxes in the loss cone (black line). There is a plateau-like region of the moderate anisotropy between these two regions (latitude ~60–62°) which is supposedly caused by a wave-particle interaction process. The morphology and occurrence of such precipitation pattern were discussed by Gvozdevsky et al. (1997). The isotropic boundary can be unambiguously defined for this auroral region crossings at 62.06° (blue vertical line). The transition (marked by green vertical line) between substantial fluxes from the plasma sheet region and nearly zero fluxes from the polar cap region can be clearly discerned at 72.3°.

Figure 1b demonstrates a more complicated precipitation pattern. There is a localized region of the isotropic precipitations at ~53.5° detached from the extended plasma sheet isotropic precipitations (latitude ~57–66°). Such localized low-latitude isotropic precipitations are attributed to the wave-particle interaction process (Søraas et al., 2013; Yahnin & Yahnina, 2007). IB was defined as an equatorial boundary of the plasma sheet isotropic precipitation at 56.9°. Note relatively high anisotropic fluxes in the polar cap for this event.

These fluxes are likely resulted from the 90° telescope contamination by the energetic neutral atoms from the ring current region (Søraas & Sorbo, 2013), and the increased flux in the loss cone was likely resulted from the solar proton event.

The pattern of the latitudinal profile in Figure 1c is somewhat similar to the previous event. There is a localized isotropic precipitation at ~61.5° detached from the bulk of the isotropic precipitations (latitude ~63.5–72°). However, for this event, the fluxes between these two regions are only slightly anisotropic (mostly <1 order of magnitude difference) and structured. An even more complicated pattern can be seen in Figure 1d. The wide region equatorward from the isotropic plasma sheet precipitations is occupied by alternating isotropic/anisotropic fluxes (latitude ~62–67.5°). Such precipitation patterns are difficult to explain by either FLC scattering or wave-particle interaction alone. In the former case, the radial profile of K parameter should have quasi-periodic variations over an extended region. In the latter case, the intense waves in specific frequency range must be persistent over a wide range of radial distances which seems to be unrealistic given complexity and energy-selectivity of the criteria for wave-related pitch angle scattering. On the other hand, we cannot rule out the possibility that low- or middle-altitude processes can disturb isotropy of precipitating fluxes (though currently such mechanisms have not been supported observationally). In these cases, the IB formed by FLC scattering is projected to the low-latitude side of the region of alternating isotropy.

Given the uncertainty of the IB definition for such events, we opted to identify the upper and low bounds in latitudes which indicate the "uncertainty interval" of IB selection. These locations are referred to as LL (low-latitude) and HL (high-latitude) IBs. They are shown in Figure 1d as a blue dashed lines. The HL IB was defined as follows: moving from the polar cap boundary to equator, we define HL IB as the last point of isotropic precipitation before the first occurrence of anisotropic precipitation. Note, however, that we ignore the localized regions of anisotropy in the close vicinity of the polar cap boundary as it can be seen in Figure 1b (latitude ~65.5–68.3°) and Figure 1c (latitude ~69.5–70.5°). We also ignored single point deviations from isotropy as it can be seen in Figure 1d (lat.~66.5 or ~67.5°). It should be mentioned that although, in general, polar cap is identified rather unambiguously as a region at high-latitudes with zero or small and constant flux level in all energy channels, it could not be observed for some orbits, for example, for those skimming along the oval. In these cases, we started our algorithm from the point of highest latitude.

Unfortunately, it is hard to formulate strict formal criteria for LL IB. We tried the following criteria. First, it is located at a lower latitude than HL IB. Next, the fluxes between HL and LL IBs should satisfy the following criteria:

1. The deviations from isotropy should be within a factor of 10.
2. There should be an alternation between isotropy and anisotropy (20% deviations from isotropy are considered as isotropic).
3. The LL IB is defined as the last point with less than factor 4 deviation from isotropy.

Even in an ideal case, IB cannot be defined with accuracy better than 0.12° along the orbit (~2-s detector resolution). In addition, there is an uncertainty of calibration for degraded detectors. These factors were taken into account during selection HL and LL IBs for all crossings of the auroral region. Since the latitudinal difference less than 0.2° cannot be visually resolved in Figure 1, the IBs are shown as single lines in three top panels where an uncertainty of IB identification was very small. In total, 2,277 pairs of HL and LL IBs have been selected. This data set also includes the time intervals before the storms. We deliberately extended the intervals in comparison to those in Table 1 rounding the time of the storm beginning to the beginning of a day. These prestorm events were included to investigate the IB evolution during a transition from prestorm to storm conditions. The number of events which are strictly inside the intervals specified in Table 1 is 1,900.

3.2. Statistical Properties of Isotropic Boundary Data Set

Having almost 2,000 storm time IBs selected, we start our analysis by exploring statistical properties of this data set. First, we investigated the response of the IB locations to a variation of the geomagnetic activity. Many authors noticed a good correlation between the proton IB latitude and Dst index (Asikainen et al., 2010; Ganushkina et al., 2005; Hauge & Søraas, 1975; Lvova et al., 2005; Søraas et al., 2002). Instead of Dst, we use here a pressure-corrected SYM-H index as it was proposed by Burton et al. (1975) : $\text{SYM-H}^* = \text{SYM-H} - 15.8\sqrt{P_{\text{dyn}}} + 20$ nT. This correction is needed because Dst and SYM-H indices include, apart from contributions from the ring and tail currents, also a contribution from the magnetopause current, which is controlled by dynamic pressure. The magnetopause currents affect the magnetic field in the dayside magnetosphere and on the

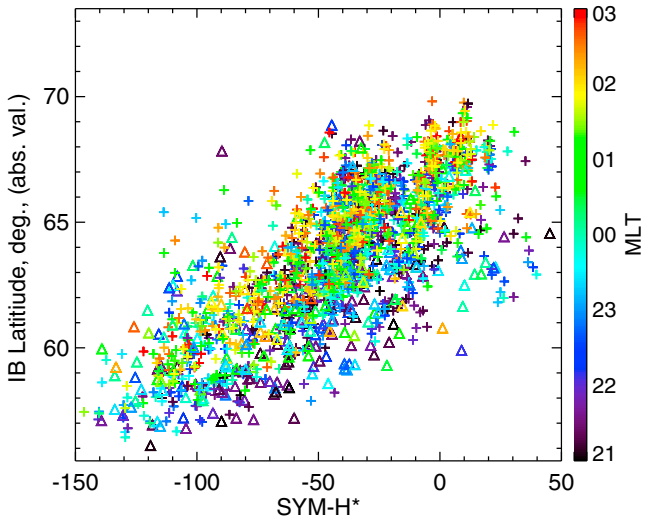

Figure 2. Absolute value of proton isotropic boundary (IB) altitude-adjusted corrected geomagnetic latitude versus SYM-H* for low-latitude IB data set. Triangles and cross symbols correspond to main and recovery phases, respectively. Color shows IB magnetic local time (MLT).

ground (Dst and SYM-H), but its influence is much less prominent at the location of the IB formation. Thus, we subtract the magnetopause current contribution using the Burton et al. (1975) equation.

Figure 2 shows the dependence of the IB AACGM latitude on SYM-H* for LL IB data set. For this figure, we only use data from those satellites for which the energy of P1 MEPED channel less than 50 keV (that is, with the detector revealing only moderate degradation, see Appendix A). The absolute value of latitude is shown to incorporate the observations from both hemispheres in one figure.

Color corresponds to MLT of IB observation (dark blue is used for the premidnight sector and green-red for the postmidnight sector). We also computed the time derivative of the smoothed SYM-H* index to analyze the relation with storm phases. To remove substorm-related short-scale variations and to smooth the original 1-min resolution data, we use Fourier transform to filter out harmonics with periods shorter than 3 h. Triangles correspond to the SYM-H* decrease periods with $dSYM\text{-}H^*/dt < -0.1$ nT/min (main phase), and crosses represent SYM-H* increase or stagnation with $dSYM\text{-}H^*/dt > -0.1$ nT/min (recovery and quiet periods). It can be seen that there are triangles in the region of positive SYM-H* values. It should be noted that pressure-corrected SYM-H is supposed to be zero or negative, and that means that Burton's pressure correction has failed for these events. Our algorithm detected a drop of SYM-H* caused by dynamic pressure drop and marked these events as a main phase. However, further in the paper, these events can be easily identified in figures (e.g., Figure 6) as we use color to show SYM-H* value.

A few results are immediately obvious from Figure 2. First one is that IBs move equatorward with SYM-H* decrease. It also can be seen that the most equatorial IBs belong to the 21–24 MLT sector (blue color), indicating a dawn-dusk asymmetry, and that the low envelope of the data point cloud is formed by triangles, which correspond to the storm main phase. Note, however, that triangles also form the upper envelop for SYM-H < -75 nT. These outliers will be further investigated below. The figure in the same format as Figure 2 but plotted for HL IB data set (not shown), displayed only minor difference with Figure 2, demonstrating that on average, the latitudinal difference between HL and LL IBs is much smaller than the latitudinal data point scatter in Figure 2. The detailed inspection showed that the difference between LL and HL IBs was >0.2° for 29%, >0.5° for 15%, and it was as large as >1° for 9% of events. We investigated the IB uncertainty dependence both on the MLT and on the geomagnetic activity. No clear dependence on MLT was found. However, the IBs with the uncertainty of >1° were more frequent during large negative SYM-H*, that is during the main phase and near the peak of the magnetic storm.

It can be seen that there are numerous outliers from the main cloud of points in Figure 2. Since such IBs can be presumably formed by different pitch angle scattering mechanism, we investigate this subgroup separately. To identify these events, for both HL and LL IB data sets we fitted the IB dependencies on SYM-H and P_{dyn}

by the following expression:

$$\Lambda_{IB} = G_0(\mathrm{MLT}) + G_1(\mathrm{MLT}) \cdot \mathrm{SYM\text{-}H} + G_1(\mathrm{MLT}) \cdot P_{dyn} \quad (2)$$

Here Λ_{IB} is an absolute value of the IB latitude, and

$$G_i(\mathrm{MLT}) = A_i + B_i \cdot \sin\left(\frac{\mathrm{MLT}}{12h}\pi\right) + C_i \cdot \cos\left(\frac{\mathrm{MLT}}{12h}\pi\right) \quad (3)$$

is the function of MLT. A_i, B_i, and C_i are the free parameters (found using standard least squares fit).

The goodness of the fit was evaluated using correlation coefficient (CC) and rms deviation (δ) between the observed IBs and those predicted by equation (2). The LL IB data set revealed higher fit quality (CC = 0.82 and $\delta = 1.57°$) as compared to the HL IB data set (CC = 0.76 and $\delta = 1.83°$). For this reason, we take LL IB data set fit as our reference model of the IB response to variation of the geomagnetic activity. Finally, we selected those anomalous events when LL IBs were located at latitudes one δ higher than those predicted by our reference model (189 events).

Next, for these selected events, we investigate how the precipitated and trapped proton fluxes vary between and around the predicted and observed IBs. Specifically, how fast the fluxes become anisotropic at latitudes lower than observed IB and whether there are any specific features associated with the predicted IB location. To superpose latitudinal profiles for all 189 anomalous events on a single axis, the normalized latitude (Λ^*) was computed for each event as following:

$$\Lambda^* = \frac{|\Lambda| - |\Lambda_{IB}^{\mathrm{observed}}|}{|\Lambda_{\mathrm{IB}}^{\mathrm{observed}}| - |\Lambda_{\mathrm{IB}}^{\mathrm{predicted}}|} \quad (4)$$

Here Λ is AACGM latitude for a particular event, $\Lambda_{\mathrm{IB}}^{\mathrm{observed}}$ and $\Lambda_{\mathrm{IB}}^{\mathrm{predicted}}$ are observed LL IB latitude and that predicted for this event using equation (2). As a result of this coordinate transformation, the latitudes of observed and predicted IBs correspond to the points $\Lambda^* = 0$ and $\Lambda^* = -1$, respectively.

For all 189 anomalous events, the percentiles of the precipitated-to-trapped flux ratio (ratio of fluxes measured by 0° and 90° MEPED P1 telescopes) were computed for a normalized latitude bin size of 0.1. Figure 3 shows these percentiles versus normalized latitude. The lines having color from dark blue to red correspond to percentiles from 10% to 90% with 10% increment. It should be noted that the fluxes can still be anisotropic at latitudes higher than observed LL IB ($\Lambda^* = 0$) because moderate anisotropy is allowed between LL and HL IBs. Nevertheless, the precipitated-to-trapped flux ratio is very close to 1 in the $\Lambda^* > 0$ region, indicating that the HL IB is located close to LL IB for a majority of selected events. On a negative side from $\Lambda^* = 0$ point, all percentiles reveal a sharp drop by a factor of 3–10 and stay at this level between $\Lambda^* = 0$ and $\Lambda^* = -1$ (that is, between observed IB and that predicted by equation (2). At latitudes lower than predicted IB latitude, the precipitated-to-trapped flux ratio decreases by 1–2 orders of magnitude.

We tried different selection criteria for the anomalous events to show that the drop of the precipitated-to-trapped flux ratio at Λ^* is not a coincidence. Only 28 events were found for stricter selection with $|\Lambda_{\mathrm{IB}}^{\mathrm{observed}}| > |\Lambda_{\mathrm{IB}}^{\mathrm{predicted}}| + 2\delta$, but the aforementioned features were even more evident (the drop of the ratio at $\Lambda^* = -1$ was steeper). Usage of the HL IB latitudes instead of $\Lambda_{\mathrm{IB}}^{\mathrm{observed}}$ also led to the similar results. These results demonstrate that although equation (2) fails to predict the IB location for these events, the predicted latitude corresponds to a special point where the pitch angle distribution of precipitating protons makes a transition from slightly anisotropic on the poleward side to strongly anisotropic one, with almost totally depleted loss cone, on its equatorial side.

For these events, the latitudinal profiles of the 0° and 90° fluxes closely remind those of the specific events investigated by Gvozdevsky et al. (1997). The authors argued that the extended region of the moderate anisotropy to the equator from IB is formed by wave-particle interaction. On the other hand, as an objection to this scenario, it should be mentioned that the intense wave-related scattering is believed to be spatially localized (around plasmapause) but the regions of moderately anisotropic precipitations occupy a broad range of latitudes in Figure 3 (larger than $\delta = 1.57°$, owing to selection criteria).

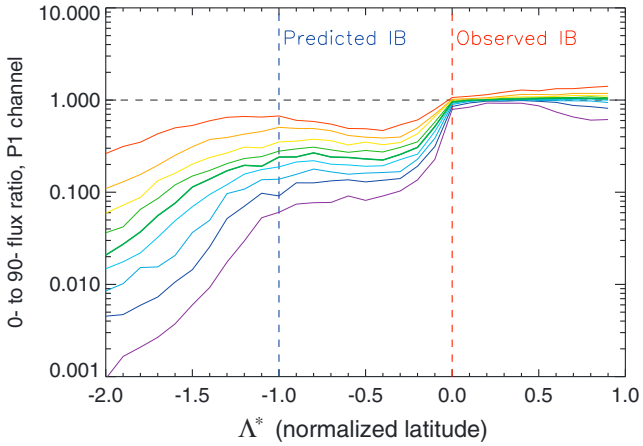

Figure 3. Percentiles of the precipitated-to-trapped flux ratio versus normalized latitude for the subset of anomalous events (see the text). The 10% – 90% percentiles are shown with 10% increment.

3.3. *K* Parameter Estimation at the Isotropic Boundary

After surveying statistical properties of our IB data set, we move to the main focus of our paper: *K* parameter estimation on IB field line. We use the empirical magnetospheric magnetic field model to trace a field line from the observed IB location at the NOAA/POES orbit to the equatorial plane and to compute the *K* parameter at the point of the model magnetic field minimum. We use the Tsyganenko and Sitnov (2005) model (hereafter TS05) that was specially designed to describe the storm time magnetosphere. The TS05 input parameters were available for 1,841 event during the storm time intervals listed in Table 1.

The model field lines were traced from both HL and LL IB locations to the equatorial plane where the curvature radius and gyroradius were estimated at the point of the magnetic field minimum. The gyroradius was estimated for the particle energy corresponding to the low-energy limit of the P1 MEPED channel taking into account the calibration factors (see Appendix A). It should be noted that for 7% of HL IBs and for 3% of LL IBs, the traced field line went outside of $r = 15R_E$ downtail, beyond TS05 model validity limit, and *K* parameter could not be estimated. Although it seems to be unrealistic and could be a result of wrong field line mapping (owning to the model inaccuracy), we do not discard these events because it would create a bias toward larger *K* values in our statistics. Indeed, the model field lines traced from the IB location can as well go closer to the Earth than the real field line. In this case, the model's inaccuracy would not lead to such big error in terms of distance (due to the influence of the strong dipole field), but the error can be much larger in terms of *K* (due to stronger magnetic field gradient). For these reasons, we just assigned $K = 0.1$ for all these events because *K* values less than 1 are expected in the distant tail (e.g., Yue et al., 2014).

Figure 4a shows the histograms of estimated *K* parameters for two data sets. Shaded black and red histograms represent HL and LL IB data sets, respectively. Figure 4b shows similar histogram but for a subset of events with the latitudinal difference between HL and LL IBs (uncertainty of IB determination) being within 0.2°, which will be referred to as "clean" IB data set (1,275 data records or ~70% of the original data set). The solid triangles mark the median values which were 10.7, 12.4, and 12.6 for HL, LL, and clean data sets, respectively. Although all three distributions were centered at $K \approx 10-13$, they are very broad. The increased number of occurrences in the first bin (especially for HL histogram) is due to the contribution of the events with $K = 0.1$ assigned by hands if traced field line goes beyond $r = 15R_E$ as discussed above. We also analyzed the dependence of the obtained *K* parameters on MLT but found no clear trend.

When attempting to interpret Figure 4 in terms of pitch angle scattering mechanism one has to take into account the following problems. First of all, the critical value of $K = 8$ was obtained by calculating particle trajectories in the idealized current sheet magnetic field configurations (like those presented by TS05), and it should be considered as a rough estimate. Its actual value may change around this number depending on the different current distribution across the current sheet (Delcourt et al., 2006), due to strong guide field (B_Y) component (Delcourt et al., 2000), because of enhanced radial *B* gradients and other deviation from simplified magnetospheric models, which may be especially significant during magnetic storms. Second, there can be uncertainties in the IB determination of different kind, which should introduce a scatter of so-determined

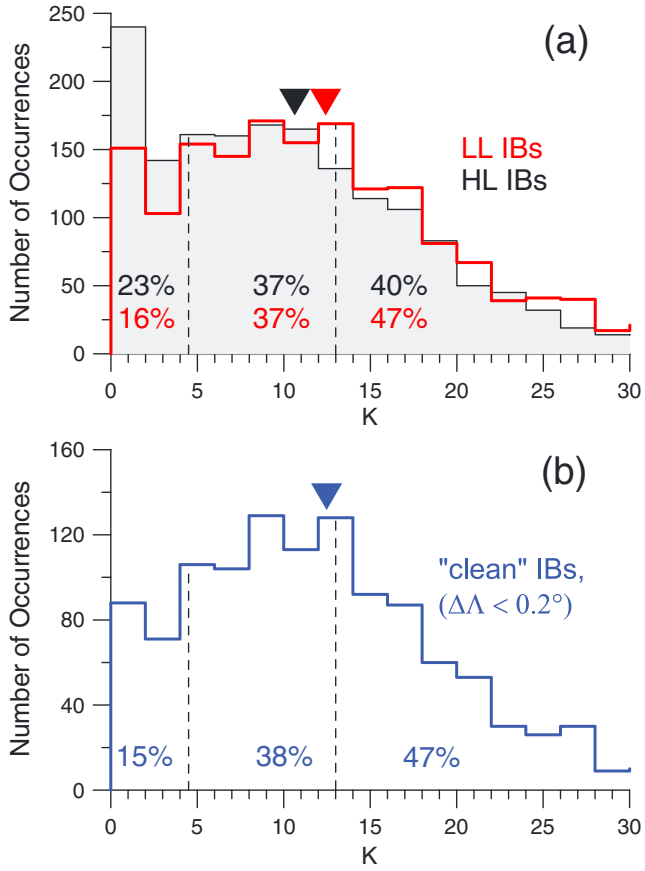

Figure 4. Histograms of K parameter estimated for observed isotropic boundary (IB) field lines using TS05. Panel (a): Shaded gray and red colors correspond to high-latitude (HL) and low-latitude (LL) IBs, respectively. Panel (b): The same as panel (a) but for clean IBs. Solid triangles mark the median values. The percentage shows the fraction of K values in the sectors separated by the black dashed lines.

(mapped) K values even if the model is perfect. Uncontrolled model deviations from reality and mapping errors also contribute to the scatter and are considered as a major source of errors. For understanding of how far the predicted equatorial IB location stays from the mapped one it could be instructive to know how the deviations of the mapped K parameter from $K = 8$ correspond to the distance between their equatorial points, particularly, to learn which K range is associated with distance difference of, say, $0.5-1R_E$. This issue can be addressed using the TS05 model.

We analyzed the radial profiles of the K parameter in TS05 model. For HL IB data set we computed the $K(r)$ profiles (at B minimum) at the MLT meridians corresponding to the IB observations. We emphasize that the choice of IB data set plays no role here because IB latitude is not used. We only use the TS05 input parameters corresponding to IB observation time (as a representation of storm time external conditions) and IB MLTs (just because they cover 21–03 MLT sector). For every profile, we defined $dR(K) = r(K) - r(K = 8)$, where $r(K)$ is a geocentric distance to the point with corresponding K parameter. dR can be plotted as a function of K. Figure 5 shows statistical distribution of the $dR(K)$ profiles for the events shown in Figure 4.

The percentiles of dR were computed for all TS05 model's $K(r)$ profiles for K parameter bin size of 1. In Figure 5, the dR percentiles ranging from 10% to 90% with 10% increment are shown versus K as blue-to-red curves. The black curve (lowest percentile) crosses $dR = -1R_E$ (bottom horizontal dashed line) line at $K \approx 13$. It means that the model's $K = 13$ point is located within 1 R_E from the point with $K = 8$ for 90% of the model's configurations. On the other hand, red curve (highest percentile) crosses $dR = +1R_E$ line at $K \approx 4.5$ meaning that the point with $K = 4.5$ is located within 1 R_E from the point with $K = 8$ for 90% of configurations. In other words, the model's estimation of K parameter between 4.5 and 13 corresponds to field lines whose equatorial points cluster in a very narrow region, being within 1 R_E from the model field line with $K = 8$.

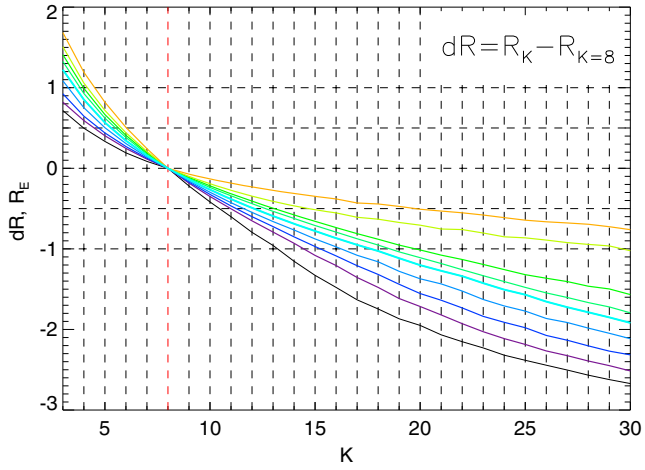

Figure 5. Statistical relation between K and dR obtained using TS05. Here dR is a distance between the point with specific K (shown on the horizontal axis) and the point with $K = 8$. Percentiles of dR are shown ranging from 10% to 90% with 10% increment.

Since the accuracy of 1 R_E is a quite optimistic estimate for the ionosphere-magnetosphere mapping, the K values within this range can be considered as supporting FLC scattering mechanism of IB formation. If the allowed field line deviation from the line with $K = 8$ is $0.5R_E$, the interval $K = 6–10$ corresponds to 90% of events fitting this stricter limit. It should be noted that even for $K = 30$, two highest percentiles in Figure 5 (red and yellow curves) are still higher than $dR = -1R_E$ line, indicating that for ~20% of events, the point with $K = 30$ is located within 1 R_E from the point with $K = 8$. These points obviously correspond to the configurations with a very strong radial gradient of the equatorial magnetic field.

Coming back to Figure 4, 37%, 37%, and 38% of events are inside $K = 4.5–13$ interval for HL, LL, and clean IB data sets, respectively. Since we found that the points with $K = 4.5–13$ are spatially very close (within 1 R_E) to $K = 8$ point in the TS05 model (see Figure 5), this percentage can be considered as a rough estimate for the occurrence rate of IBs formed by FLC scattering. However, we cannot be sure that the K values outside this interval necessarily correspond to IBs formed by some other mechanism because there is no information on the actual model mapping accuracy for these events, which could be much worse than $1R_E$. Next step will be to evaluate the deviations of the model configuration from the real one and attempt to correct the mapped K values.

Since the TS05 model is statistical in nature, its deviation from the real configuration for a particular event can be large, especially during dynamic storm events. For this reason, the independent control of the model accuracy is needed. To evaluate the model accuracy for a particular event, we compare the magnetic field measurements at the THEMIS probes with those predicted by the models. To control the model in the region of the expected IB projection, we selected those events in which the THEMIS probes were within $r = 4–10R_E$ and within ±1 h in MLT from observed IB. This selection reduced a number of IBs in our data set to 244.

Which measurable parameters are suitable to control the model performance? The IB formation is controlled by $B_Z^2/(dB_X/dz)$ (equation (1)). However, the deviation of the solar wind velocity from the radial direction can be as large as several degrees, and the current sheet can undergo strong large-scale flapping oscillations. It means that the model prediction of the current sheet position (Z coordinate) and B_X can often be unreliable. On the other hand, for the thin current sheet (1-D-like) configurations, B_Z is nearly constant across the current sheet. It means that even if the model prediction of the current sheet position is wrong, the model estimations of B_Z are less affected. Since the equatorial B_Z is the main parameter which controls the mapping and it enters equation (1) as a second-degree power exponent, we use the difference of the B_Z^{OBS} and B_Z^{MOD} as a proper indicator of the model accuracy (GSM coordinates are used).

There were often 2 or 3 THEMIS probes in conjunction with IB ($r = 4–10R_E$, ±1 h from IB). In such cases, we use the average over all probes in the region:

$$\Delta B_Z = \langle B_Z^{OBS} - B_Z^{MOD} \rangle = \frac{1}{N} \sum_{i=1,\ldots,N} \left(B_{Zi}^{OBS} - B_{Zi}^{MOD} \right) \quad (5)$$

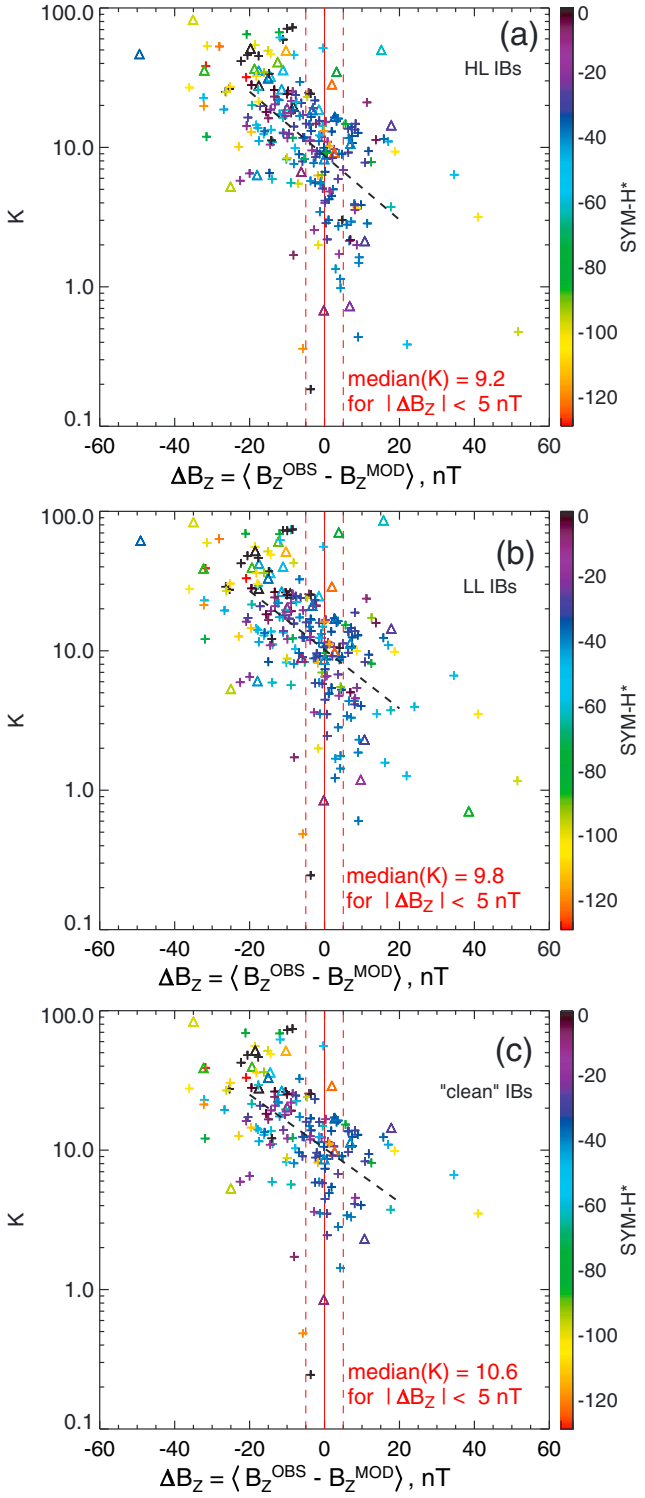

Figure 6. *K* parameter versus the model B_Z error. Triangles and cross symbols correspond to main and recovery phases, respectively. *K* parameter estimations are made for high-latitude isotropic boundaries (IBs) (a) and low-latitude IBs (b) and clean IBs (c).

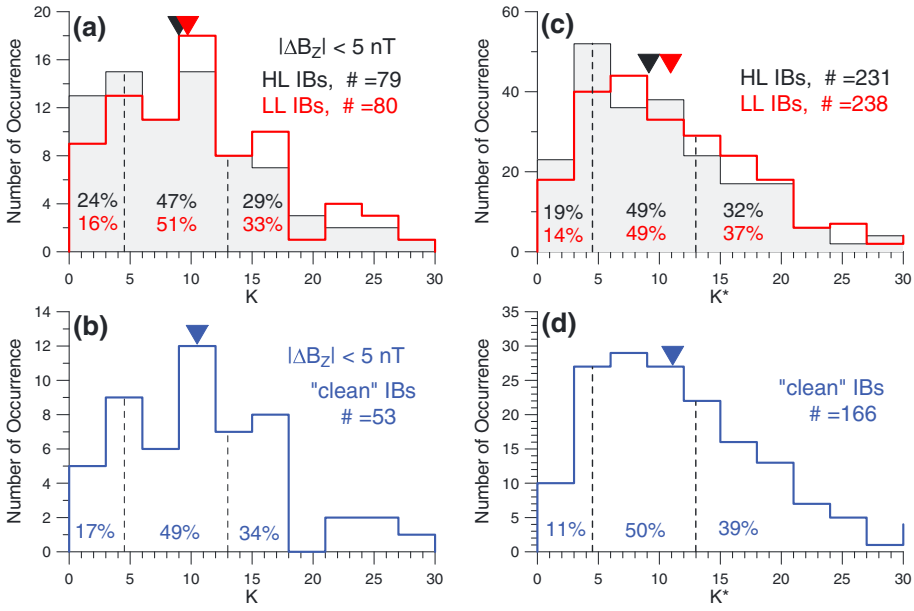

Figure 7. Panels (a) and (b): the histograms of K parameter for events with $|\Delta B_Z| < 5$ nT. Panels (c) and (d): histograms of K parameter mathematically shifted to $\Delta B_Z = 0$ line. The format is the same as in Figure 4. HL = high latitude; LL = low-latitude; IBs = isotropic boundaries.

Figure 6 shows the TS05 model estimations of the mapped K parameter against ΔB_Z for HL (a), LL (b), and clean (c) IB data sets. The clean IB data set supported by THEMIS observation comprises only 169 events. Color corresponds to SYM-H* as shown on the right (positive SYM-H* is shown by black). Triangle and cross symbols correspond to the main and recovery phases as defined in section 3.1. Negative ΔB_Z corresponds to the events when model B_Z is stronger than real B_Z, that is, the model overestimates K parameter (see equation (1)). In addition, it means that the model is understretched and the equatorial projection of the IB field line is closer to the Earth than the real field line, and again K parameter is overestimated. The opposite is true for positive ΔB_Z: the model underestimates K parameter for such events. The expected ΔB_Z control is obvious in all three panels of Figure 6; the clouds of points obviously have the negative slopes.

We selected those events in which the modeled and measured magnetic field agree to within 5 nT and computed the median of K parameter for the events. This region is marked in Figure 6 by the red vertical dashed lines and the median K values are shown in red font at the bottom of the panels. It can be seen that median values vary between 9.2 and 10.6, being close to $K = 8$ expected for the FLC scattering mechanism. Figures 7a and 7b show the histograms of the K parameter for the events with $|\Delta B_Z| < 5$ nT for the HL and LL (panel a) and clean (panel b) IB data sets. If compared to Figure 4, the scatter of K values was reduced, with the percentage of events with $K > 13$ changing from 40%–47% in Figure 4 to 29%–34% in Figures 7a and 7b. We checked how the percentage of the events with $K < 13$ (which can be attributed to the FLC scattering mechanism) depended on the allowed model accuracy. For LL IB data set, we found 64%, 68%, 76%, and 77% for $|\Delta B_Z|$ less than 10, 5, 2, and 1 nT, respectively. The number of events for these four subsets was 138, 80, 37, and 22, respectively. This sequence is converging to ~80% of the events with $K < 13$ for $\Delta B_Z = 0$. The similar numbers were obtained for HL IBs, and clean IBs data sets (except for the fact that there are fewer events in the clean data set).

However, it should be also noted that the majority of events in the region of the high model accuracy correspond to the periods of low and moderate disturbances (SYM-H* > −40 nT). In addition, the main phase is represented by eight points only and $K > 13$ for five of them. On the other hand, there are more events corresponding to active storm periods in the region of large negative ΔB_Z. Now we attempt to correct

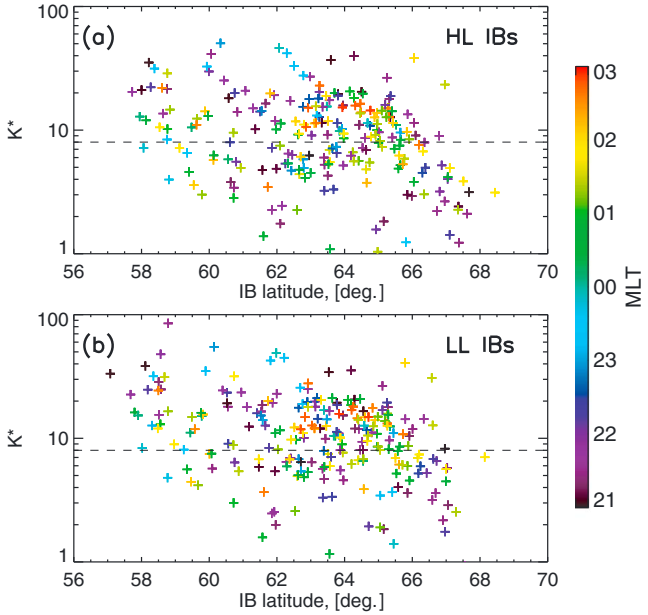

Figure 8. Corrected K values versus absolute value of isotropic boundary (IB) latitude for high-latitude (HL) (a) and low-latitude (LL) (b) data sets. Dashed lines mark $K = 8$ level. Color shows IB magnetic local tide (MLT).

the K-distributions. Since the K parameter values in Figure 6 demonstrate clear dependence on ΔB_Z, we try to subtract this trend mathematically shifting K values to the $\Delta B_Z = 0$ line. We fit the points with $|\Delta B_Z| < 20$ nT using a linear regression in log-linear scale:

$$\log K = C_1 + C_2 \cdot \Delta B_Z \tag{6}$$

C_1 and C_2 are free parameters found using standard least squares minimization. The resulting fits are shown in all panels of Figure 6 by black dashed line. Using the obtained C_2 parameter, the K values can be corrected as

$$K^* = K \cdot \exp\left(-C_2 \Delta B_Z\right) \tag{7}$$

Here and throughout the paper the asterisk symbol is used to differentiate the K parameter corrected using equation (7) (K^*) from original uncorrected value (K). Equation (7) essentially performs a projection of the points onto the $\Delta B_Z = 0$ line along a direction parallel to the dashed line, and this correction was applied to all K values irrespective of ΔB_Z. Note that correcting factor exponentially depends on ΔB_Z, demonstrating a high sensitivity of the estimated K parameter to the model error in B_Z. For example, the model's B_Z error of 5 nT leads to ~30% error of estimated K.

Figures 7c and 7d show the histograms of K^* in the same format as panels (a) and (b). It can be seen that the percentages of events for three selected intervals of K parameter are quite similar to those obtained if only events with $|\Delta B_Z| < 5$ nT are considered. $K^* > 13$ was found for ~30%–40% of events; the percentage is 10% lower than that in Figure 4. The difference is even more evident for higher K values, the percentage of events with $K > 20$ is almost twice lower (~ 15%) in Figures 7c and 7d as compared to ~25% in Figure 4. The difference is even more pronounced for events with $K > 30$, 5% and 14% in Figures 7d and 4b, respectively. This means that considerable part of high K events in the uncorrected K distributions are false numbers, caused by the understretched magnetic configuration in the model. At the same time, the distributions in Figures 7c and 7d still peak within $K = 4.5$–13, with median values of K^* being 9.2, 10.9, and 11.1 for HL, LL, and clean data sets, respectively.

Figure 8 shows the estimated K^* values against the IB latitude for HL (top) and LL (bottom) IB data sets. Color corresponds to MLT. For IBs located at latitudes ~59–66°, the estimated K^* values show no dependence on IB latitude. However, the K^* values are systematically higher than 8 for IBs located lower than ~59° and systematically lower than 8 for those located higher than ~66°. This does not necessarily mean that IBs at latitudes

Table 2
Selected Events Categorized According to the Predicted K Parameter

Satellite	Date/Time	SYM-H*	K	IB Latitude	Color
NOAA-15	2013-06-29/06:16:24	−112	0.48	−63.43	Blue
NOAA-17	2012-07-16/00:24:46	−100	2.4	−65.06	Blue
NOAA-18	2012-04-24/02:31:45	−124	9.7	−59.44	Red
NOAA-18	2012-07-15/17:52:06	−113	8.15	−60.00	Red
NOAA-19	2013-06-01/11:10:25	−91	7.0	−62.37	Red
NOAA-19	2013-06-01/13:58:47	−82	9.6	62.41	Red
NOAA-17	2012-10-01/08:36:28	−96	23.9	−60.52	Green
NOAA-19	2012-04-24/02:25:48	−123	28.8	−58.35	Green

lower than 59° are formed in the region of higher K. Indeed, the method which was used to correct for the model bias (equation (7)) is quite primitive and can fail for large ΔB_Z. We did find that ΔB_Z was greater than 10 nT for all IBs at latitudes lower than 59°. In addition, K^* is systematically lower for IBs located at high latitudes, indicating that the model fails to describe these configurations (no other explanation can be devised for low K^* values). It can be speculated that the model is accurate for regular configurations with IB latitudes in ~60–66° range, but it becomes biased for extreme events just as for IB latitudes lower than 59° so for IB latitudes higher than 66°. It is important that there is no clear dependence of K^*-parameter on MLT for these data sets, while this dependence is rather obvious in Figure 2 for IB latitude. We also plotted the histograms of K^* for different MLT sectors (not shown), but again, no distinct difference was found. It should be noted that this is exactly what expected for the FLC scattering mechanism of IB formation: $K \approx 8$ irrespective of where IB is projected to.

Finally, we inspected the K values for the high-latitude outlier events which were selected in section 3.2. Unfortunately, there were no suitable THEMIS observations available for the majority of these events and the correction of the K values could not be applied. Since the results presented in section 3.2 imply that the latitude predicted by equation (2) ($\Lambda^* = -1$ in Figure 3) corresponds to the low-latitude boundary of some pitch angle scattering mechanism, we also investigated the conditions in the equatorial region for these points as well as for observed IBs. The median K values of 4.5 and 19.3 were found for the observed and predicted IBs, respectively. For observed IBs, K values within 4.5–13 range was found in 42% of events. On the other hand, for predicted IBs, the fraction of such events was only 21%. That is, if the observed and predicted IBs are compared, these are rather observed IBs which agree with the FLC scattering mechanism of IB formation. The somewhat lower K values for these events are likely caused by the mapping errors.

3.4. Detailed Analysis of Selected Events

To gain further insight about what causes the diversity of the K values, we present a detailed analysis of a few selected events. Figures 7a and 7b show that for the events when the TS05 model is in a good agreement with magnetic field measurements the distribution of K parameter, though still broad, peaks at $K \approx 9$–11. However, for these events (region marked by vertical dashed lines in Figure 6), there are only 9–10 points (9 for HL and 10 for LL IB data sets) corresponding to the storm peak periods with SYM-H* < −80 nT and these points are scattered between $K \approx 1$ and $K \approx 30$ (not shown). Of these 10 events, we selected those belonging to one of three groups according to their K value: $K > 20$, $6 < K < 10$, and $K < 3$. The central K interval corresponds to the K values expected for FLC scattering. The values of $K = 6$ and 10 were chosen as those corresponding to the points located within $0.5R_E$ from the point with $K = 8$ (see Figure 5). Two other K intervals correspond to K values that cannot be easily explained using FLC scattering mechanism. The IBs with $K > 20$ can be hypothetically formed by the wave-particle interaction, but we do not have a plausible explanation for the events with $K < 3$ other than inaccurate model predictions. Luckily, the same events were selected for both LL and HL data sets. These events are listed in Table 2. All parameters correspond to LL IBs, but those for HL IBs were very close.

We analyze these events in details trying to figure out what is the difference between the evens with K expected for the FLC scattering mechanism and other events. The columns of Table 2 are (from left to right) satellite name, IB observation time, the SYM-H index, K parameter at the IB field line computed using TS05, the observed IB latitude, and the last column is explained later. We inspected all available observations

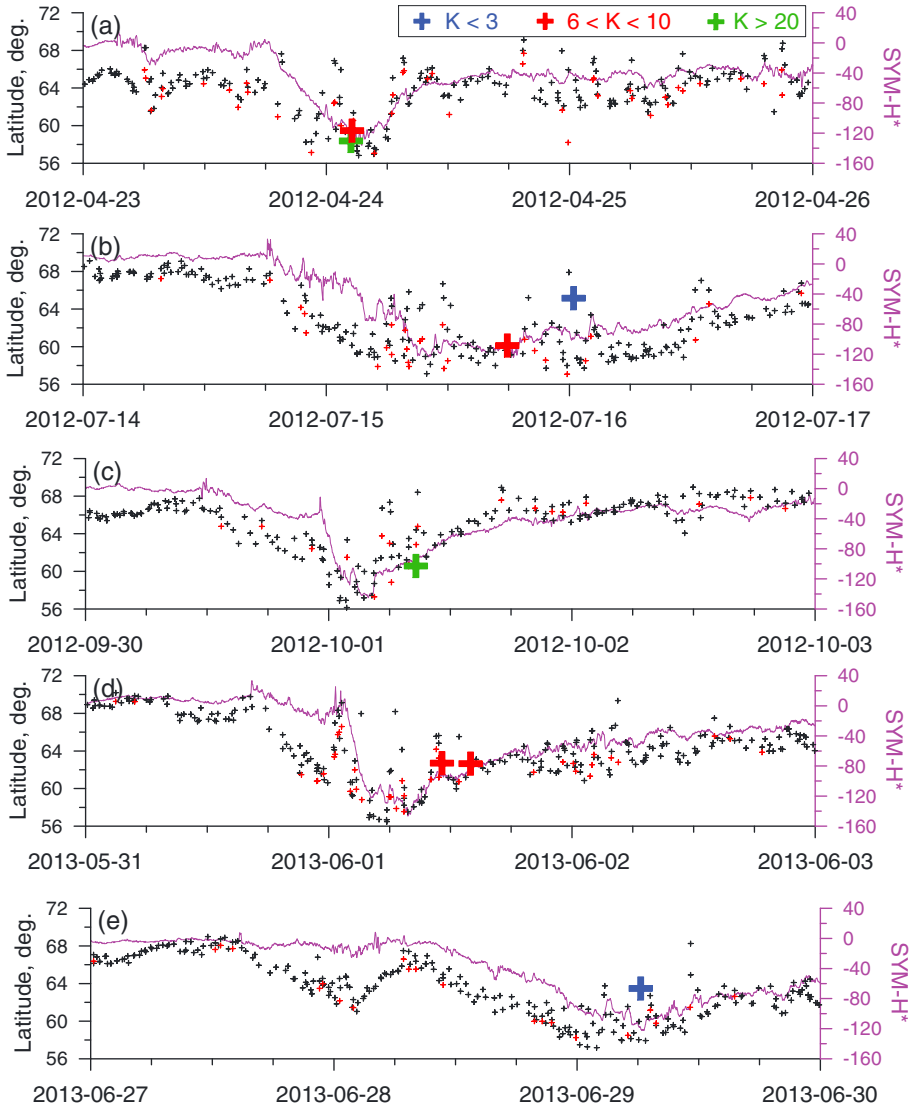

Figure 9. The SYM-H* (magenta curve) with the overlapped latitude of observed high-latitude and low-latitude isotropic boundary (absolute value, black and red crosses, respectively). Thick colored crosses correspond to the isotropic boundary latitudes for events listed in Table 2 (see text).

during these events in an attempt to find the characteristics which would be discriminating between these three groups. However, nothing specific was found in THEMIS observations, model predictions, or shape of latitudinal profiles of the low-altitude fluxes except for one event which will be discussed later.

Figure 9 shows survey plots for the storms when IBs listed in Table 2 were observed. Each panel of Figure 9 shows the SYM-H* index (magenta curve, the axis is on the right) with the overlapped latitudes of observed HL IBs (black crosses, the axis is on the left). LL IBs are shown by small red crosses if the difference in latitude with respect to HL IB was greater than 0.5°. IBs listed in Table 2 are shown by thick colored cross symbols. Red, green, and blue colors correspond to $6 < K < 10$ (expected for the FLC scattering), $K > 20$ (possibly wave-particle interaction), and $K < 3$ (wrong mapping or some unknown mechanism of the pitch angle distribution transformation), respectively.

It can be seen that the IB latitudes follow the variations of SYM-H* closely except for transient periods when the IB latitude shows up and down excursions (e.g., 23 April 2012/22:00 to 24 April 2012/02:00). A prominent difference between HL and LL IBs can be seen during these IB excursions. Two IBs with $K < 3$ (blue thick cross symbols) lie clearly above the main sequence of IBs. Two IBs with $K > 20$ (green thick cross symbols), though

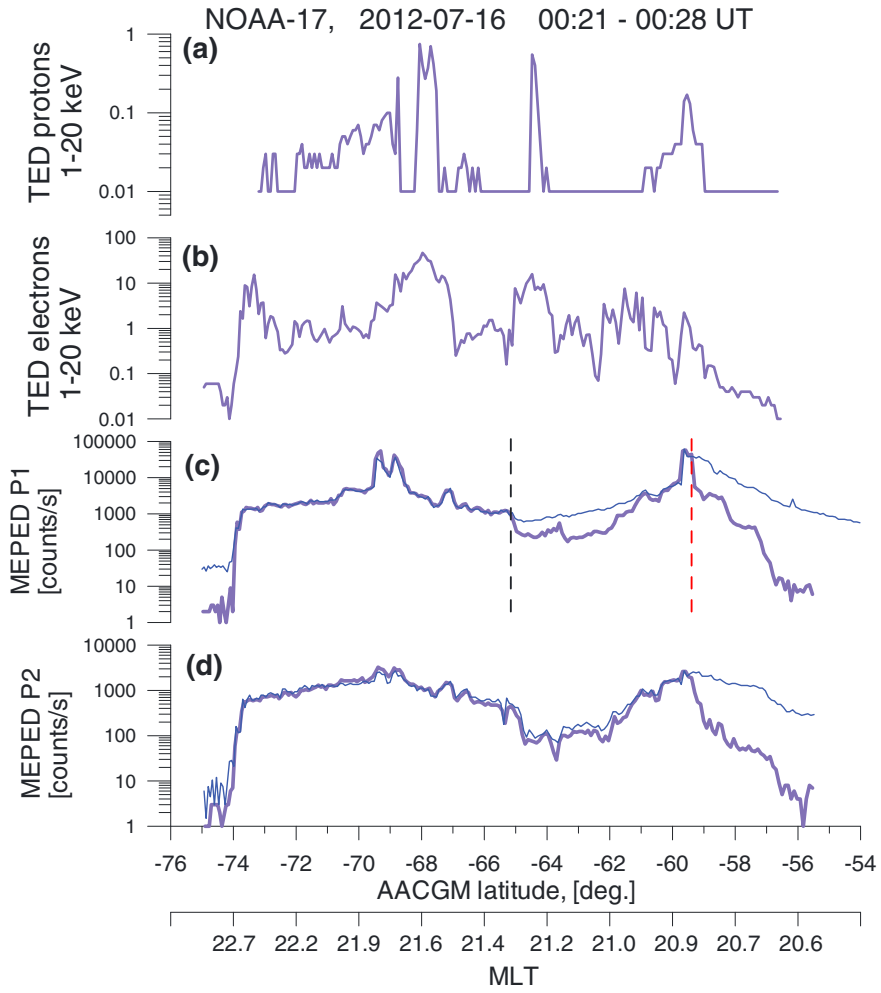

Figure 10. The latitudinal profiles of the observed parameters. (a) Integrated proton energy flux ($E = 1–20$ keV), (b) electron energy flux ($E = 1–20$ keV), (c) integrated proton number fluxes ($E > 45$ keV), (d) integrated proton number fluxes ($E > 80$ keV). Black dashed vertical line marks the isotropic boundary position. Red dashed vertical line marks the equatormost isotropic boundary (see text). MEPED = Medium Energy Proton and Electron Detector; AACGM = altitude-adjusted corrected geomagnetic.

less evident, seem to lie at the bottom envelope of the main IB sequence. Finally, IBs with K values in 6–10 range appear to lie on the main IB sequence or at a bit higher latitudes, as those in Figure 9d.

In almost all events in Table 2 latitudinal profiles of the low-altitude fluxes looked typical; a gradual increase of the fluxes from the polar boundary toward IB, then the anisotropic region where 0° flux still persists at the level roughly 1 order of magnitude below 90° flux level before diminishing sharply at ~55–59°. However, the event 16 July 2012/00:24 (second line in Table 2) was apparently anomalous.

The latitudinal profiles of the fluxes measured at low altitude for this event are presented in Figure 10. These observations were made by NOAA-17 satellite at ~21 MLT during the early recovery phase. Figures 10a and 10b present the precipitated energy fluxes of thermal (< 20 keV) protons and electrons, respectively (measured by TED electrostatic analyzer). Figure 10c shows precipitated (thick) and trapped (thin) proton fluxes in P1 energy channel ($E > 45$ keV) of MEPED detector. The location of HL IB is marked by the black dashed vertical line. The LL IB (not shown) was defined very close to HL IB for this event. Figure 10d shows precipitated and trapped proton fluxes in P2 channel ($E > 80$ keV). It can be seen in Figure 10c that there is a region of isotropic precipitations to the equator from IB. The two isotropy regions are separated by anisotropic precipitations (1 order of magnitude difference between 0° and 90° fluxes). It can be argued that LL IB should be placed at the equatorial side of the equatormost isotropic precipitations (red dashed line). However, one of the requirements for LL IB selection was that the flux between HL and LL IBs should reveal alternating isotropy

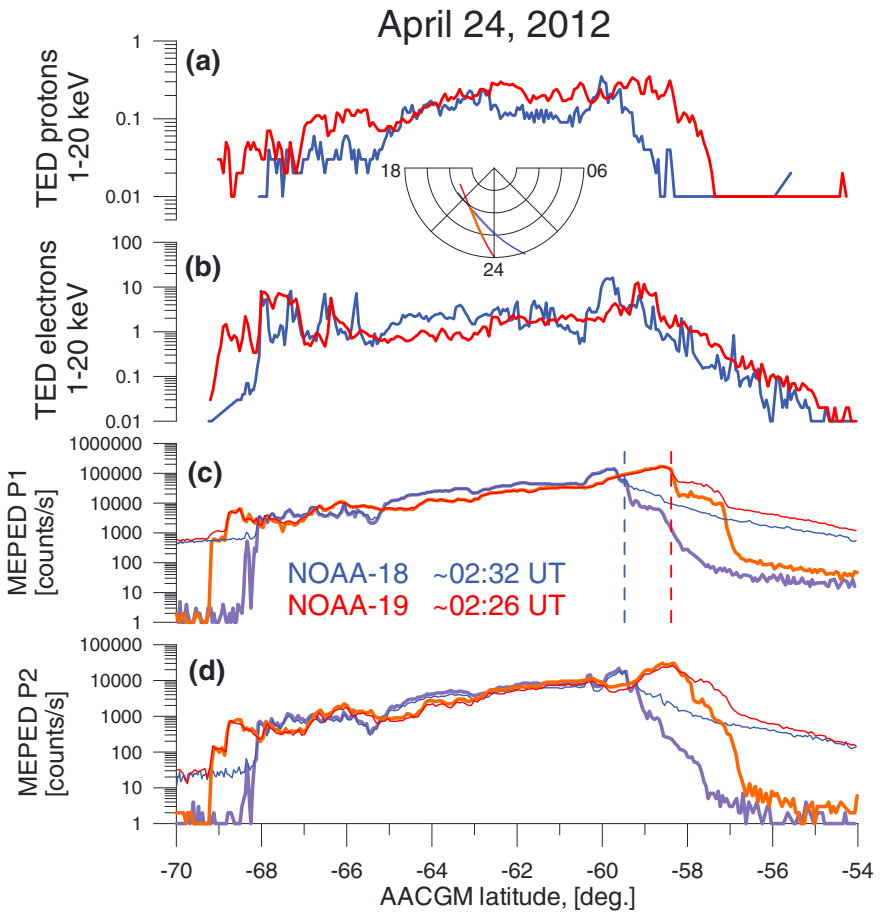

Figure 11. The latitudinal profiles of the observed parameters for two consecutive auroral oval crossings separated by ~6-min NOAA-18 and NOAA-19 observations are shown in blue and red, respectively. The insert between (a) and (b) panels shows the segments of the orbits. MEPED = Medium Energy Proton and Electron Detector; TED = Total Energy Detector; AACGM = altitude-adjusted corrected geomagnetic.

(see section 3.1), but this was not the case for the present event. The equatormost isotropic precipitations of energetic ions ($E > 45$ keV) coincide with localized precipitations of thermal ions ($E < 20$ keV, Figure 10a). These features fit the definition of Localized Precipitation of Energetic Protons type 2 structure associated with EMIC waves at plasmapause (Yahnin & Yahnina, 2007; Yahnina et al., 2003). Interestingly, that the anisotropy region between −65° and −61° of latitude, so obvious in Figure 10c, can be barely discerned in Figure 10d for the protons with higher energies (P2 channel). Note also that all proton structures are embedded into the electron plasma sheet precipitation (see Figure 10b). The K parameter estimated for the IB field line using TS05 was rather small ($K = 2.4$). Figure 9b shows that this IB (blue cross) is located at significantly higher latitude than adjacent IBs. In fact, a few adjacent IBs are located at 58–60°, just where the detached region of isotropic precipitation is seen in Figure 10c. Unfortunately, the adjacent IBs were not in conjunction with THEMIS or there was a large difference between the model field and magnetic measurements and accurate K parameter estimate could not be done. Using TS05, we traced the field line from the point of the equatormost boundary of isotropic precipitation (marked by red dashed vertical line in Figure 10c) located at −59.4° latitude. K value of 10.6 was found for the equatorial projection of this field line which is not so much different from $K = 8$ expected for the FLC scattering mechanism.

Table 2 shows that two events occurred for approximately the same time on 24 April 2012. For the second event, $K = 28.8$ was found. Since these two IBs were observed at approximately the same time (~6-min difference) and approximately the same MLT (~1-h difference), we plot both latitudinal profiles in one figure. Figure 11 shows the observations of two satellites in the same format as Figure 10. The insert between Figures 11a and 11b shows the segments of the orbits. Both satellites crossed the auroral oval from the equator

to the pole. The IB was first detected by NOAA-19 at 23.4 MLT, and ~6 min later it was detected by NOAA-18 at 0.2 MLT. It can be seen that the equatorial part of the latitudinal profiles has a similar shape but is displaced by ~1° of latitude. The TS05 model projected one IB to the region with $K \approx 10$ and another to the region with $K \approx 29$.

It is rather difficult to separate spatial and temporal effects in this event. The low-altitude observations can be interpreted as a poleward IB movement or a strong azimuthal dependence (IB at 23 MLT is at ~1° higher latitude in comparison to that at midnight). Note, however, that the situation definitely was rather dynamic because the satellites crossed the polar cap boundary at the same MLT but it was displaced by ~1° equatorward for NOAA-18 passage. There were three THEMIS probes in conjunction with low-altitude satellites. The probes were located near the midnight ($Y_{GSM} = -0.3 - -0.2R_E$) between $r = 4R_E$ and $r = 5.5R_E$ in the region of strong magnetic field ($B_Z = 60-100$ nT) and strong magnetic field gradient. It is interesting that the TS05 model overestimated B_Z at the innermost probe position and underestimated it at two outer probes. That means that $B_Z^{OBS} - B_Z^{MOD}$ is negative for innermost probe and positive for outer probes. That is, the model overestimates the B_Z gradient. When ΔB_Z is computed using equation (5), the contributions from different probes partly cancel each other out. If ΔB_Z were computed with absolute values of the sum members, ΔB_Z values would be 6.9 and 4.5 nT for NOAA-19 and NOAA-18, respectively. In such a case, the IB with $K = 28.8$ (NOAA-19) would not pass our criterion for the 5 nT model agreement with the measurements. In addition, MLT conjunction between THEMIS probes and low-altitude satellite is worse for NOAA-19 IB (~1 h difference in MLT).

4. Discussion

Our study was initially motivated by two reasons. One was an expectation that during magnetic storms, the generally enhanced level of wave activity plays an increasing role in proton precipitation and, possibly, in the formation of the proton isotropic boundary (IB). Another reason was the recently raised doubts about the role of FLC-scattering as a dominant mechanism of IB formation, particularly, a large percentage of high K-parameter values found at the equatorial end of the IB field line, whereas the $K \sim 8$ was expected in case of the FLC-related mechanism (Ilie et al., 2015; Sergeev, Chernyaeva, Angelopoulos, et al., 2015). It should be noted that both papers used the models in the same way like we use in our study, but they had a small number (only a few dozen) events at their disposal.

Studying the IB-related K values in ~ 2,000 events, we have found that although the distribution is rather broad, it is centered not far from the theoretical estimate (median(K) < 13 in all plots of Figure 4). Moreover, we found that the points with K values inside 4.5 – 13 interval are located in the narrow region within $1R_E$ from the $K = 8$ location as dictated by strong radial B gradients in the quasi-dipole magnetic field. Such events constitute a large part of all events, being more than a third of all events in the uncorrected K distribution (Figure 4) and about a half in the corrected K distribution (Figure 7).

For a smaller subset of events (~250), we were also able to control independently the accuracy of model predictions by comparing them to magnetic observations at the THEMIS probes approximately conjugated with low-altitude IBs. Like in previous similar comparisons based on geostationary spacecraft and IB observations (Donovan, Jackel, Voronkov, et al., 2003), we found a very clear correlation between ΔB_Z and the K parameter estimations (Figure 6). Using this dependence, the K values were tentatively corrected to take into account the model deviations from the actual magnetic field observations. We use asterisk symbol to differentiate the corrected K^* value from original uncorrected K value. After being corrected, K^* distribution was centered at $K^* \sim 10$ (Figure 7). This is not as terribly different from the corrected average value of $K^* \sim 17$ (for 30 keV proton IB) and $K^* \sim 13$ (for 80 keV proton IB) found by Sergeev, Chernyaeva, Angelopoulos, et al. (2015), but it is very far from median value $K \sim 33$ of Ilie et al. (2015). We remind that global MHD model was used for mapping in the latter paper. It should be noted that a good agreement of the modeled and observed B_Z does not fully guarantee an accurate estimation of K parameter because equation (1) also includes dB_X/dZ in the denominator. Unfortunately, multispacecraft configurations allowing the estimation of dB_X/dZ in the current sheet center at the proper range of radial distance occur quite rarely. We emphasize that sufficient statistics and appropriate tools allowing to exclude a systematic bias in model predictions are both very essential in this kind of studies, and in our paper, we attempted to improve in both aspects.

Another effect of the correction was that the K^* distribution also became more narrow, especially at large K^* values; the percentage of events with $K^* > 30$ was reduced to 5%, twice as small compared to those found before the correction (Figure 4). The demonstration that large width of K distributions comes mainly from inaccurate model predictions is another important conclusion of our study. This is consistent with findings by Sergeev, Chernyaeva, Angelopoulos, et al. (2015) who used a more sophisticated model adapted to the data of the THEMIS spacecraft cluster and found that samples with $K > 32$ occurred only in the data set in which the spacecraft distance from the IB field line was greater than $2R_E$ (a very rigorous requirement). The existence of large scatter into the lower K region is one more argument in favor of model inaccuracies as a basic origin of strong scatter in K space: the pitch angle scattering amplitude is known to grow exponentially with decreasing K, so the pitch angle scattering amplitude is normally ~10 times larger at $K \sim 4$ than at $K \sim 8$ (Delcourt et al., 1996).

To a large extent, the inaccurate B field representation should be the main origin of large K^* scatter which still remains after the correction was applied. This is especially obvious during active conditions when the magnetic configuration can be drastically different at nearby locations (say, inside and outside of the plasma bubbles/Burst Bulk Flows), when large temporal variations occur (see an example in Figure 11 and rapid variations of the IB latitude in Figure 9) and when the B field values and its gradients inevitably deviate from their smooth representation in the average empirical models. At the same time, the theoretical threshold of strong scatter can also vary depending on the unusual steep radial B_Z gradients, etc. Its very large changes were demonstrated in current sheet geometries for different transverse distributions of electric current density (Delcourt et al., 1996, 2006) or even for additional guide component (B_Y) of the magnetic field (Delcourt et al., 2000). It should be noted that the analytical functions, defining a geometry of the current sheet in the empirical models, are rather simple and, in fact, are not necessarily physically self-consistent with thermal plasma (Zaharia & Cheng, 2003). Some efforts toward developing a plasma-magnetic field consistent magnetospheric model and using it for studying pitch angle scattering mechanism were recently made (see Yue et al., 2014, and references therein), but at present, this model still lacks a flexibility in the representation of different states of the magnetospheric activity. The actual range of possible K threshold variations for ~30–80 keV proton IB still remains unspecified, and this definitely requires future studies.

There are another two important results indicating that wave-particle interaction plays a minor role, if any, in the IB formation. First, we found no appreciable dependence of the K^* parameter distribution on MLT, whereas the IB latitude reveals rather clear dependence in Figure 2. However, if the waves played an essential role, such dependence would be expected because occurrences of the EMIC waves (Halford et al., 2010; Usanova et al., 2012) and anomalous IB dispersion (Dubyagin et al., 2013) both reveal strong dependence on MLT. On the other hand, it might be speculated that negative result was due to a limited number of events ~250 or/and because the IBs on the dusk flank (15–21 MLT) were not considered. Second, the K^* parameters estimations do not reveal visible dependence on the IB latitude, except for events with IB located at extremely low or high latitudes (<59° or >66°), for which the K parameter correction could fail. The findings imply that the FLC scattering is a persistent mechanism of IB formation operating in a variety of magnetospheric conditions.

An additional contribution to large K scattering may also come from the uncertainty in the IB identification itself, and this is what we also addressed in our study. We found that the uncertainty of IB selection is highly critical for ~10% of events. However, even uncertainty as small as ~0.5°, found for ~15% of events, can lead to a significant uncertainty in estimated K values. Although it does not affect the main statistical results of our study, it can be of key importance for case studies (as demonstrated in Figure 10). The problem of the IB identification during storm activity deserves to be addressed in the future studies, possibly, using supportive information from other detectors/telescopes.

Although our results clearly emphasize the dominant role of FLC-scattering for IB formation, still two indications can be interpreted as rare manifestations of the wave-particle interaction in the IB vicinity. The first indication is high K values found for IB latitude lower than ~59°. Since the wave-related precipitations were observed mostly at low latitudes (Yahnin & Yahnina, 2007), these IB could be formed by wave-particle interaction process. Less than 10% of IBs are located at latitude lower than 59°, but they are of special interest because they all correspond to SYM-H* minimum period (Figure 2). Second, we discovered a specific class of events, when the empirical formula (equation (2) describing the IB latitude variation with SYM-H and P_{dyn} fails to predict the IB location but instead predicts the location of the equatorial cutoff of the moderately anisotropic precipitation in the loss cone, mapped to the region of high K parameter (see Figure 3). For these events, the real IBs are located at significantly higher latitudes. The latitudinal profiles of the 0° and 90° fluxes closely

remind those for the specific events investigated by (Gvozdevsky et al., 1997) and called Low-Latitude Proton Precipitation. The most plausible mechanism explaining the moderately anisotropic precipitations between the observed and predicted IBs is a moderate scattering by the electromagnetic waves. It is very puzzling why, in some cases, equation (2), which was obtained using the large data set of IBs mostly formed by FLC scattering, predicts the location of some specific boundary formed by wave-particle interaction process. As a possible explanation, it can be speculated that the wave-related IBs constitute a larger part of all IBs than it seems from the analysis of K distribution. However, not willing to speculate on this topic further, we leave this puzzle to future research. The estimate for occurrence rate of the wave-related IBs can be also found as a percentage of events with $K > 13$ in Figure 7, which is 30%–40%.

5. Conclusions

Using a large data set of the low-altitude IB observations (~2,000 IB determinations during nine geomagnetic storms), we used the TS05 model to estimate the adiabaticity parameter K (ratio of the magnetic field line curvature radius to the particle gyroradius) at the equatorial part of the IB field line during nine moderate geomagnetic storms. The concurrent magnetic field measurements onboard THEMIS probes in the equatorial magnetotail were used to control the TS05 deviations from the real magnetic configuration. It was found that the TS05 configuration is systematically understretched during the intervals of an SYM-H minimum, and this leads to K parameter overestimation. For small group of events with THEMIS data available, we introduced a tentative K parameter correction which compensates the model bias based on B_Z difference between model prediction and THEMIS observation. This correction resulted in a significant reduction of the statistical scatter in the corrected K^* parameter distribution, demonstrating the importance of the independent control of the model accuracy for this kind of studies. Contrary to the findings of Sergeev, Chernyaeva, Angelopoulos, et al. (2015) and Ilie et al. (2015), we found the median K parameter value of 9–12 being close to $K = 8$ expected for the FLC scattering mechanism of IB formation. Numerical tests with the TS05 model showed that K values in 4.5–13 interval correspond to the points located within $1R_E$ from the $K = 8$ field line; correspondingly, we consider the $K < 13$ values as those indicating the FLC mechanism. Different estimates give percentages of such events between 60% and 80%. The remaining 20%–40% provide an upper estimate for the occurrence of IBs formed by the wave-particle interaction process. Finally, we did not find any appreciable dependence of the K parameter distribution on MLT, whereas the IB latitude reveals rather clear MLT asymmetry. Although the IB latitude undergoes dramatic variations during storm time, the K parameter distribution also does not show a clear dependence on the IB latitude, except for events with IB located at extremely low latitudes (<59°). Summarizing our findings we conclude that the pitch angle scattering on the curved field lines is a dominant mechanism of the energetic proton isotropic boundary formation operating in a variety of magnetospheric conditions.

Appendix A: NOAA/POES Proton MEPED Detector Calibrations

The proton SEM-2 MEPED detector measures fluxes in a few energy channels (P1, P2, P3, …). There are two solid-state telescopes for each of energy channels. One telescope points to local zenith (it is referred to as 0° telescope) and another points along the satellite orbit (referred to as 90° telescope). At auroral latitudes, the 0° telescope detects ion fluxes precipitating into a loss cone. The 90° telescope detects fluxes of the locally trapped ions. The proton MEPED detector is subjected to degradation which leads to an increase of the low-energy threshold (Asikainen et al., 2012; Ødegaard et al., 2016; Sandanger et al., 2015). The shift of the low-energy threshold is described using the calibration factor α so that $E_{\text{corrected}} = \alpha \cdot E_{\text{nominal}}$. Asikainen et al. (2012) provided the α values up to the year 2011. Sandanger et al. (2015) used different method and provided the α values for later years (not for all satellites). There is some (moderate) discrepancy between the α values obtained in these two works. Taking into account all these results, we use the α values as given in Table A1 to estimate the low-energy limit for P1 proton 0° detector. However, the 90° telescope is subjected to even stronger degradation. It means that its low-energy limit is even higher than that for 0° detector.

Generally, a recomputation of the fluxes to the nominal energy range requires the information about the spectrum (Asikainen et al., 2012), and in any case, this procedure is rather complex. Instead of doing this, we use the P1 0° telescope flux without any correction (just assuming that the flux corresponds to the energy of the channel estimated using α factors). However, since $E_{\text{corrected}}$ is different for 0° and 90° telescopes, the 90° flux must be scaled to the 0° telescope energy range. The algorithm of such scaling was developed

Table A1
α Values for the 0° Telescope for P1 Energy Channel

Year \Satellite	01	02	15	16	17	18	19
2011	1.0	1.09	2.16	1.53	1.47	1.01	1.00
2012	1.0	1.12	2.20	1.57	1.51	1.04	1.03
2013	1.0	1.13	2.22	1.59	1.53	1.05	1.04

Note. The satellite index is specified in the top row.

in Dubyagin et al. (2013); however, it worked well only for certain oval crossings. The possible reason for the poor algorithm performance can be a contamination of the MEPED data by energetic neutral atoms from ring current regions (a level of contamination is different for inbound and outbound oval crossings) (Søraas et al., 2003; Søraas & Sorbo, 2013). In addition, the detector also responds to heavier ions (see section 4 of Søraas et al. (2002), for more details), which are ubiquitous during storms. For this reason, we develop a simplified approach. We determine correction separately for every auroral oval crossing. It is assumed that correction for 90° flux can be represented as a constant multiplier. We search for such multiplier that the resulting 90° flux fits the 0° flux in the region where the isotropy is expected. This region was defined as a region poleward from the maximum of the 0° flux (so called b2i-boundary; Newell et al., 1996). The 90° flux calibration factor was computed as a median(flux0/flux90) in the isotropy region.

Acknowledgments
The NOAA/POES particle data were downloaded form National Geophysical Data Center website: https://www.ngdc.noaa.gov/stp/satellite/poes/index.html. THEMIS magnetic field data were loaded and calibrated using official software at http://themis.ssl.berkeley.edu. The solar wind and IMF data were downloaded from the OMNI database from the GSFC/SPDF OMNIWeb interface at http://omniweb.gsfc.nasa.gov. The 1-min resolution SYM-H and AE, AL, indices were provided by the World Data Center for geomagnetism, Kyoto (http://wdc.kugi.kyoto-u.ac.jp/). The precomputed input parameters for Tsyganenko and Sitnov (2005) model were downloaded from http://geo.phys.spbu.ru/~tsyganenko/modeling.html. The part of the research done by N. Ganushkina and S. Dubyagin has received funding from the European Union Seventh Framework Programme (FP7/20072013) under grant agreement 606716 SPACESTORM and from the European Union Horizon 2020 Research and Innovation programme under grant agreement 637302 PROGRESS. N. Ganushkina thanks the International Space Science Institute in Bern, Switzerland, for their support of the international teams on "Analysis of Cluster Inner Magnetosphere Campaign data, in application the dynamics of waves and wave-particle interaction within the outer radiation belt" and "Ring current modeling: Uncommon Assumptions and Common Misconceptions". Support for N. Ganushkina at the University of Michigan was provided by NASA research grants NNX14AF34G, NNX17AI48G, NNX17AB87G, and 80NSSC17K0015.

References

Angelopoulos, V. (2008). The THEMIS mission. *Space Science Reviews*, *141*, 5–34. https://doi.org/10.1007/s11214-008-9336-1

Asikainen, T., Maliniemi, V., & Mursula, K. (2010). Modeling the contributions of ring, tail, and magnetopause currents to the corrected *Dst* index. *Journal of Geophysical Research*, *115*, A12203. https://doi.org/10.1029/2010JA015774

Asikainen, T., Mursula, K., & Maliniemi, V. (2012). Correction of detector noise and recalibration of NOAA/MEPED energetic proton fluxes. *Journal of Geophysical Research*, *117*, A09204. https://doi.org/10.1029/2012JA017593

Auster, H. U., Glassmeier, K. H., Magnes, W., Aydogar, O., Baumjohann, W., Constantinescu, D., et al. (2008). The THEMIS fluxgate magnetometer. *Space Science Reviews*, *141*, 235–236. https://doi.org/10.1007/s11214-008-9365-9

Baker, K. B., & Wing, S. (1989). A new magnetic coordinate system for conjugate studies at high latitudes. *Journal of Geophysical Research*, *94*(A7), 9139–9143. https://doi.org/10.1029/JA094iA07p09139

Büchner, J., & Zelenyi, L. M. (1989). Regular and chaotic charged particle motion in magnetotaillike field reversals: 1. Basic theory of trapped motion. *Journal of Geophysical Research*, *94*(A9), 11,821–11,842. https://doi.org/10.1029/JA094iA09p11821

Burton, R. K., McPherron, R. L., & Russell, C. T. (1975). An empirical relationship between interplanetary conditions and *Dst*. *Journal of Geophysical Research*, *80*(31), 4204–4214. https://doi.org/10. 1029/JA080i031p04204

Delcourt, D. C., Malova, H. V., & Zelenyi, L. M. (2006). Quasi-adiabaticity in bifurcated current sheets. *Geophysical Research Letters*, 33, L06106. https://doi.org/10.1029/2005GL025463

Delcourt, D. C., Sauvaud, J.-A., Martin, R. F. Jr., & Moore, T. E. (1996). On the nonadiabatic precipitation of ions from the near-Earth plasma sheet. *Journal of Geophysical Research*, *101*(A8), 17,409–17,418. https://doi.org/10.1029/96JA01006

Delcourt, D. C., Zelenyi, L. M., & Sauvaud, J. A. (2000). Magnetic moment scattering in a field reversal with nonzero *BY* component. *Journal of Geophysical Research*, *105*(A1), 349–359. https://doi.org/10.1029/1999JA900451

Donovan, E. F., Jackel, B., Klumpar, D., & Strangeway, R. (2003). Energy dependence of the isotropy boundary latitude. In *Proceedings of atmospheric studies by optical methods* (Vol. 92, pp. 11–14). Finland: Sodankylä Geophysical Observatory Publications.

Donovan, E. F., Jackel, B. J., Voronkov, I., Sotirelis, T., Creutzberg, F., & Nicholson, N. A. (2003). Ground-based optical determination of the b2i boundary: A basis for an optical MT-index. *Journal of Geophysical Research*, *108*(A3), 1115. https://doi.org/10.1029/2001JA009198

Dubyagin, S., Ganushkina, N., Apatenkov, S., Kubyshkina, M., Singer, H., & Liemohn, M. (2013). Geometry of duskside equatorial current during magnetic storm main phase as deduced from magnetospheric and low-altitude observations. *Annales Geophysicae*, *31*, 395–408. https://doi.org/10.5194/angeo-31-395-2013

Erlandson, R. E., & Ukhorskiy, A. J. (2001). Observations of electromagnetic ion cyclotron waves during geomagnetic storms: Wave occurrence and pitch angle scattering. *Journal of Geophysical Research*, *106*(A3), 3883–3895. https://doi.org/10.1029/2000JA000083

Evans, D. S., & Greer, M. S. (2000). Polar orbiting environmental satellite space environment monitor: 2. Instrument descriptions and archive data documentation (*NOAA Tech. Memo*). Boulder, CO: OAR SEC-93, NOAA.

Fraser, B. J., & Nguyen, T. S. (2001). Is the plasmapause a preferred source region of electromagnetic ion cyclotron waves in the magnetosphere? *Journal of Atmospheric and Solar-Terrestrial Physics*, *63*(11), 1225–1247.

Ganushkina, N. Y., Pulkkinen, T. I., Kubyshkina, M. V., Sergeev, V. A., Lvova, E. A., Yahnina, T. A., et al. (2005). Proton isotropy boundaries as measured on mid- and low-altitude satellites. *Annales Geophysicae*, *23*, 1839–1847. https://doi.org/10.5194/angeo-23-998 1839-2005

Gary, S. P., Thomsen, M. F., Yin, L., & Winske, D. (1995). Electromagnetic proton cyclotron instability: Interactions with magnetospheric protons. *Journal of Geophysical Research*, *100*(A11), 21,961–21,972. https://doi.org/10.1029/95JA01403

Gilson, M. L., Raeder, J., Donovan, E., Ge, Y. S., & Kepko, L. (2012). Global simulation of proton precipitation due to field line curvature during substorms. *Journal of Geophysical Research*, *117*, A05216. https://doi.org/10.1029/2012JA017562

Gvozdevsky, B. B., Sergeev, V. A., & Mursula, K. (1997). Long lasting energetic proton precipitation in the inner magnetosphere after substorms. *Journal of Geophysical Research*, *102*(A11), 24,333–24,338. https://doi.org/10.1029/97JA02062

Halford, A. J., Fraser, B. J., & Morley, S. K. (2010). EMIC wave activity during geomagnetic storm and nonstorm periods: CRRES results. *Journal of Geophysical Research*, *115*, A12248. https://doi.org/10.1029/2010JA015716

Hauge, R., & Søraas, F. (1975). Precipitation of > 115 keV protons in the evening and forenoon sectors in relation to the magnetic activity. *Planetary and Space Science*, *23*(8), 1141–1154.

Horne, R. B., & Thorne, R. M. (1993). On the preferred source location for the convective amplification of ion cyclotron waves. *Journal of Geophysical Research*, *98*(A6), 9233–9247. https://doi.org/10.1029/92JA02972

Ilie, R., Ganushkina, N., Toth, G., Dubyagin, S., & Liemohn, M. W. (2015). Testing the magnetotail configuration based on observations of low-altitude isotropic boundaries during quiet times. *Journal of Geophysical Research: Space Physics*, *120*, 10,557–10,573. https://doi.org/10.1002/2015JA021858

Imhof, W. L., Reagan, J. B., & Gaines, E. E. (1977). Fine-scale spatial structure in the pitch angle distributions of energetic particles near the midnight trapping boundary. *Journal of Geophysical Research*, *82*(32), 5215–5221. https://doi.org/10.1029/JA082i032p05215

Imhof, W. L., Reagan, J. B., & Gaines, E. E. (1979). Studies of the sharply defined L dependent energy threshold for isotropy at the midnight trapping boundary. *Journal of Geophysical Research*, *84*(A11), 6371–6384. https://doi.org/10.1029/JA084iA11p06371

Keika, K., Takahashi, K., Ukhorskiy, A. Y., & Miyoshi, Y. (2013). Global characteristics of electromagnetic ion cyclotron waves: Occurrence rate and its storm dependence. *Journal of Geophysical Research: Space Physics*, *118*, 4135–4150. https://doi.org/10.1002/jgra.50385

Kennel, C. F., & Petschek, H. E. (1966). Limit on stably trapped particle fluxes. *Journal of Geophysical Research*, *71*(1), 1–28. https://doi.org/10.1029/JZ071i001p00001

Kozyra, J. U., Cravens, T. E., Nagy, A. F., Fontheim, E. G., & Ong, R. S. B. (1984). Effects of energetic heavy ions on electromagnetic ion cyclotron wave generation in the plasmapause region. *Journal of Geophysical Research*, *89*(A4), 2217–2233. https://doi.org/10.1029/JA089iA04p02217

Kubyshkina, M. V., Sergeev, V. A., & Pulkkinen, T. I. (1999). Hybrid Input Algorithm: An event-oriented magnetospheric model. *Journal of Geophysical Research*, *104*(A11), 24,977–24,993. https://doi.org/10.1029/1999JA900222

Liang, J., Donovan, E., Ni, B., Yue, C., Jiang, F., & Angelopoulos, V. (2014). On an energy-latitude dispersion pattern of ion precipitation potentially associated with magnetospheric EMIC waves. *Journal of Geophysical Research: Space Physics*, *119*, 8137–8160. https://doi.org/10.1002/2014JA020226

Lvova, E. A., Sergeev, V. A., & Bagautdinova, G. R. (2005). Statistical study of the proton isotropy boundary. *Annales Geophysicae*, *23*, 1311–1316. https://doi.org/10.5194/angeo-23-1311-2005

Newell, P. T., Feldstein, Y. I., Galperin, Y. I., & Meng, C.-I. (1996). Morphology of nightside precipitation. *Journal of Geophysical Research*, *101*(A5), 10,737–10,748. https://doi.org/10.1029/95JA03516

Ødegaard, L.-K., Nesse Tyssoy, G. H., Sandanger, M. I., Stadsnes, J., & Søraas, F. (2016). Space Weather impact on the degradation of energetic proton detectors. *Journal of Space Weather and Space Climate*, *6*, 1–15. https://doi.org/10.1051/swsc/2016020

Pulkkinen, T. I., Baker, D. N., Pellinen, R. J., BÃijchner, J., Koskinen, H. E. J., Lopez, R. E., et al. (1992). Particle scattering and current sheet stability in the geomagnetic tail during the substorm growth phase. *Journal of Geophysical Research*, *97*(A12), 19,283–19,297. https://doi.org/10.1029/92JA01189

Sandanger, M. I., Ødegaard, L. K. G., Nesse Tyssøy, H., Stadsnes, J., Søraas, F., Oksavik, K., & Aarsnes, K. (2015). In-flight calibration of NOAA POES proton detectors-Derivation of the MEPED correction factors. *Journal of Geophysical Research: Space Physics*, *120*, 9578–9593. https://doi.org/10.1002/2015JA021388

Sergeev, V. A., Chernyaeva, I. A., Angelopoulos, V., & Ganushkina, N. Y. (2015). Magnetospheric conditions near the equatorial footpoints of proton isotropy boundaries. *Annales Geophysicae*, *33*, 1485–1493. https://doi.org/10.5194/angeo-33-1485-2015

Sergeev, V. A., Chernyaeva, S. A., Apatenkov, S. V., Ganushkina, N. Y., & Dubyagin, S. V. (2015). Energy-latitude dispersion patterns near the isotropy boundaries of energetic protons. *Annales Geophysicae*, *33*, 1059–1070. https://doi.org/10.5194/angeo-33-1059-2015

Sergeev, V. A., Malkov, M., & Mursula, K. (1993). Testing the isotropic boundary algorithm method to evaluate the magnetic field configuration in the tail. *Journal of Geophysical Research*, *98*(A5), 7609–7620. https://doi.org/10.1029/92JA02587

Sergeev, V. A., Sazhina, E. M., Tsyganenko, N. A., Lundblad, J. A., & Søraas, F. (1983). Pitch-angle scattering of energetic protons in the magnetotail current sheet as the dominant source of their isotropic precipitation into the nightside ionosphere. *Planetary and Space Science*, *31*, 1147–1155.

Søraas, F., Aarsnes, K., Oksavik, K., & Evans, D. S. (2002). Ring current intensity estimated from low-altitude proton observations. *Journal of Geophysical Research*, *107*(A7), 1149. https://doi.org/10.1029/2001JA000123, 2002

Søraas, F., Lundblad, J. Å., & Hultqvist, B. (1977). On the energy dependence of the ring current proton precipitation. *Planet Space Science*, *25*, 757–763.

Søraas, F., Laundal, K. M., & Usanova, M. (2013). Coincident particle and optical observations of nightside subauroral proton precipitation. *Journal of Geophysical Research: Space Physics*, *118*, 1112–1122. https://doi.org/10.1002/jgra.50172

Søraas, F., Oksavik, K., Aarsnes, K., Evans, D. S., & Greer, M. S. (2003). Storm time equatorial belt—An "image" of RC behavior. *Geophysical Research Letters*, *30*(2), 1052. https://doi.org/10.1029/2002GL015636

Søraas, F., & Sorbo, M. (2013). Low altitude observations of ENA from the ring current and from the proton oval. *Journal of Atmospheric and Solar-Terrestrial Physics*, *99*, 104–110. https://doi.org/10.1016/j.jastp.2012.10.003

Tsyganenko, N. A., & Sitnov, M. I. (2005). Modeling the dynamics of the inner magnetosphere during strong geomagnetic storms. *Journal of Geophysical Research*, *110*, A03208. https://doi.org/10.1029/2004JA010798

Usanova, M. E., Mann, I. R., Bortnik, J., Shao, L., & Angelopoulos, V. (2012). THEMIS observations of electromagnetic ion cyclotron wave occurrence: Dependence on AE, SYMH, and solar wind dynamic pressure. *Journal of Geophysical Research*, *117*, A10218. https://doi.org/10.1029/2012JA018049

Usanova, M. E., Mann, I. R., & Darrouzet, F. (2016). EMIC waves in the inner magnetosphere. In A. Keiling, D.-H. Lee, & V. Nakariakov (Eds.), *Low-Frequency Waves in Space Plasmas*. Hoboken, NJ: John Wiley. https://doi.org/10.1002/9781119055006.ch5

Wang, C.-P., Zaharia, S. G., Lyons, L. R., & Angelopoulos, V. (2013). Spatial distributions of ion pitch angle anisotropy in the near-Earth magnetosphere and tail plasma sheet. *Journal of Geophysical Research: Space Physics*, *118*, 244–255. https://doi.org/10.1029/2012JA018275

Xiong, Y., Yuan, Z., & Wang, J. (2016). Energetic ions scattered into the loss cone with observations of the cluster satellite. *Annales Geophysicae*, *34*, 249–257. https://doi.org/10.5194/angeo-34-249-2016, 2016

Yahnina, T. A., Yahnin, A. G., Kangas, J., Manninen, J., Evans, D. S., Demekhov, A. G., et al. (2003). Energetic particle counterparts for geomagnetic pulsations of Pc1 and IPDP types. *Annales Geophysicae*, *21*, 2281–2292. https://doi.org/10.5194/angeo-21-2281-2003

Yahnin, A. G., & Yahnina, T. A. (2007). Energetic proton precipitation related to ion-cyclotron waves. *Journal of Atmospheric and Solar-Terrestrial Physics*, *69*, 1690–1706.

Yuan, Z., Xiong, Y., Wang, D., Li, M., Deng, X., Yahnin, A. G., et al. (2012). Characteristics of precipitating energetic ions/electrons associated with the wave-particle interaction in the plasmaspheric plume. *Journal of Geophysical Research*, *117*, A08324. https://doi.org/10.1029/2012JA017783

Yue, C., Wang, C.-P., Lyons, L., Liang, J., Donovan, E. F., Zaharia, S. G., & Henderson, M. (2014). Current sheet scattering and ion isotropic boundary under 3-D empirical force-balanced magnetic field. *Journal of Geophysical Research: Space Physics*, *119*, 8202–8211. https://doi.org/10.1002/2014JA020172

Zaharia, S., & Cheng, C. Z. (2003). Can an isotropic plasma pressure distribution be in force balance with the T96 model field? *Journal of Geophysical Research*, *108*(A1), 1412. https://doi.org/10.1029/2002JA009501